ONE-DIMENSIONAL (1-D) NANOSTRUCTURED METAL OXIDES

FOR CATALYTIC OXIDATION OF HYDROCARBONS

A DISSERTATION

SUBMITTED TO THE DEPARTMENT OF

MATERIALS SCIENCE AND ENGINEERING

AND THE COMMITTEE ON GRADUATE STUDIES

OF STANFORD UNIVERSITY

IN PARTIAL FULFILLMENT OF THE REQUIREMENTS

FOR THE DEGREE OF

DOCTOR OF PHILOSOPHY

Yunzhe Feng

August 2012

This dissertation is online at: http://purl.stanford.edu/rs129bc6364

I certify that I have read this dissertation and that, in my opinion, it is fully adequate in scope and quality as a dissertation for the degree of Doctor of Philosophy.

Xiaolin Zheng, Primary Adviser

I certify that I have read this dissertation and that, in my opinion, it is fully adequate in scope and quality as a dissertation for the degree of Doctor of Philosophy.

Alberto Salleo, Co-Adviser

I certify that I have read this dissertation and that, in my opinion, it is fully adequate in scope and quality as a dissertation for the degree of Doctor of Philosophy.

Bruce Clemens

Approved for the Stanford University Committee on Graduate Studies.

Patricia J. Gumport, Vice Provost Graduate Education

This signature page was generated electronically upon submission of this dissertation in electronic format. An original signed hard copy of the signature page is on file in University Archives.

Abstract

Catalytic oxidation of hydrocarbons has been intensively studied, with the purpose of minimizing emissions of pollutants and facilitating the combustion process. Noble metals, such as platinum and palladium, are the most effective catalysts for the oxidation of hydrocarbons. However, the limited supply of these noble metals imposes a need for developing alternative catalysts. Transition metal oxides are attractive alternatives due to their high thermal stability and low cost.

Previous studies of metal oxide catalysts have focused on metal oxide nanoparticles (NPs) supported on porous substrates, such as Al_2O_3, ZrO_2 and spinel-type (AB_2O_4) supports. Although the dispersed metal species over large surface area have shown much higher activity than the bulk metal oxide, there are several limitations. First, interactions between the support and NPs at high temperatures impede the fundamental understanding of the catalytic properties of individual NPs, and limit their application conditions. Moreover, the solid supports limit the loading of NPs because NPs tend to aggregate at large loadings, leading to a decrease in catalytic activity.

Herein, one-dimensional (1-D) nanostructured metal oxide were directly grown on metal mesh substrates and used as catalysts for hydrocarbons oxidation. The 1-D nanostructured catalysts benefits from reduced interaction with the substrates, great flexibility in increasing the catalyst loading, and convenience in tuning the surface

chemistry for higher catalytic activity, thus exhibit comparable or better catalytic activity and stability compared to the supported NPs.

As one of the most active metal oxide catalysts, CuO was used as a model system to demonstrate the effectiveness of the 1-D nanostructured metal oxide catalysts. CuO NWs have been grown on Cu mesh by solid phase diffusion and applied to catalyze methane oxidation reactions. The CuO NWs have shown comparable or even better activity and stability than the supported CuO NPs. Moreover, owing to the fact that the NWs were exposed on the substrate surface and easy to access, two methods were used to tune the NWs for enhanced catalytic activity. The first one was to reduce the CuO NWs to more active Cu_2O NWs by H_2 plasma, which has shown 20% increase activity for CH_4 oxidation reactions and several times higher activity for CO oxidation reactions. The kinetics study have shown that the bulk oxygen diffusion in Cu_2O was faster, which could be one of the reasons for higher activity of Cu_2O than that of CuO. The second tuning method was to decorate the CuO NWs with more active NP materials, such as Co_3O_4 and noble metals with a newly developed simple, fast and general sol-flame method. After the Co_3O_4 decoration, the CuO NWs surface was uniformly and densely covered by Co_3O_4 NP-chain structures, with large NP loading, high surface area and minimal aggregation, resulting in times higher activity in catalyzing CH_4 oxidation. Moreover, this sol-flame method is a general method to decorate NWs with various NPs, and even to dope NWs with dopants for desirable properties. Given the generality and simplicity of the sol-flame methods, it can be applied to not only catalysis, but also other important application areas, such as lithium ion battery, supercapacitor and photoelectrochemical devices.

In addition, to incorporate Cu and Co, the most active metal oxide catalyst Co_3O_4 was grown as 1-D structure on stainless steel mesh with the Cu^{2+} ion enhanced ammonia-evaporation-induced synthesis method. The synergetic effects of Cu and Co in catalytic process were studied, which have shown that the Cu^{2+} improved the nucleation and growth process of 1-D Co_3O_4, however, the catalytic activity is mainly from the Co species.

Acknowledgements

I would not have the opportunity to write the acknowledgements of my Ph. D. dissertation today if others had not helped me along the way in many respects. I am profoundly grateful of all those people who have supported and helped me through my Ph. D. career at Stanford University.

First and foremost, I would like to express my deepest thanks to my research advisor, Prof. Xiaolin Zheng, for her remarkable guidance, support and encouragement throughout my Ph.D. life at Stanford. Her enthusiasm in science, creativity in research and encouragement in students make her not only a great scientist but also a nice mentor to work with. Her keen scientific insights and serious working attitude will always be a source of inspiration for my future career. I would like to thank her for leading me into this exciting field, for giving me freedom in work, for teaching me all the academic skills, for having faith in me when I struggled, and for supporting me strongly along the way. I feel really lucky to have had Xiaolin as my advisor.

I would also like to thank Prof. Alberto Salleo, Prof. Bruce Clemens, Prof. Thomas Jaramillo and Prof. Mark Brongersma for serving in my defense committee. Their comments and suggestions at my thesis defense motivated the future work in the lab and helped me write the dissertation better. In particular, I would like to thank Prof. Alberto Salleo and Prof. Bruce Clemens for their time reading my thesis.

non-research related issues has made my life easier at Stanford and helped me focus on research. Thanks to Larry Candido, Fi Verplanke, Tori Gottlieb, Jane Edwards, Cita Levita, Perry Thoorsell, Nichole Sparks, Chris Crismon and Brittany Voelker.

Many other people were also of great help to me. Many friends and fellow classmates have inspired me via many discussions. I am so honored to have been able to work with and become acquainted with so many brilliant and talented people. I look forward to seeing all the great things I am sure these people would accomplish. I also would wish them all the best in the future.

Last but not least, I would like to thank my parents for their unconditional love and support. They have made countless sacrifices to ensure that I could freely pursue my career. I feel so lucky and proud to have parents like them. As the only child of them, I regret that my attending graduate school in United States has made it more difficult to visit home and spend time with them. I thank their understanding and hope to be able to make up those lost memories in the future.

Table of Contents

List of Tables

List of Figures

Chapter 1.   Introduction

1.1.   Heterogeneous catalysts

1.1.1. Definitions

A catalyst is a substance that increases the rate of a reaction without modifying the overall standard Gibbs free energy change in the reaction. The catalyst is both a reactant and product of the reaction. The process is called catalysis. Catalysis can be classified as homogeneous catalysis, in which only one phase is involved, and heterogeneous catalysis, in which the reaction occurs at or near an interface between phases [1]. The heterogeneous catalysts hold vital importance in world economy, which have been widely used in numerous fields in the chemical, food, pharmaceutical, automobile and petrochemical industries [2]. It has been estimated that 90% of all chemical processes use heterogeneous catalysts [3].

The heterogeneous catalyst is normally a solid material, so that it is easy to separate from the gas and/or liquid reactants and products of the overall catalytic reaction, which is the main advantage of heterogeneous catalyst over the homogeneous one. The key of a heterogeneous catalyst is the active sites at the solid surface, so catalyst typically has a high-surface area material (e.g., 10–1000 m^2 g^{-1}), and it is usually desirable to maximize the number of active sites per reactor volume.

Catalysis by solid materials has been observed quantitatively at temperatures ranges from 78 K to 1500 K and pressures from 10^{-9} to 10^3 bar, with reactants in the

gas phase or in solvents. The activity of a catalyst is defined by the number of revolutions of the catalytic cycle per unit time, given in units of turnover rate (TOR) or turnover frequency (TOF) [4]. TOFs of commonly used heterogeneous catalysts are on the order of one per second. The life of the catalyst can be defined as the number of turnovers observed before the catalyst ceases to operate at an acceptable rate, which must be larger than a unit, otherwise the substance used is not a catalyst but a reagent. Catalyst life can either be short, as in catalytic cracking of oil, or very long, corresponding to as many as 10^9 turnovers in ammonia synthesis [5]. To simplify, the light-off curves are often used to evaluate catalytic activity, too.

Dumesic et. al. summarized the key attributes of a good catalysts, which are usually used as the criteria to evaluate catalysts [5]:

- The catalyst should exhibit good **selectivity** for production of the desired products and minimal production of undesirable byproducts.
- The catalyst should achieve adequate **rates of reaction** at the desired reaction conditions of the process (remembering that achieving good selectivity is usually more important than achieving high catalytic activity).
- The catalyst should show **stable performance** at reaction conditions for long periods of time, or it should be possible to regenerate good catalyst performance by appropriate treatment of the deactivated catalyst after short periods.
- The catalyst should have **good accessibility** of reactants and products to the active sites such that high rates can be achieved per reactor volume.

1.1.2. Characterizations of heterogeneous catalysts

a).   Surface areas and porosity

For the solid catalysts, the reactions occur on the surface, thus the surface area is considered to be an important requirement in catalyst characterization, which is related to the total active sites and the overall activity. In addition, the pore size distribution can affect the molecular transportation and reaction pathways; therefore, it is another important parameter to investigate. Physisorption of gases, such as N_2 and Ar, is used to determine the surface area and porosity, with the BET method [6] to measure the surface area, molecular simulation or non-local density functional theory (NLDFT) [7-9]to quantify the mesoporous structure.

b).   Particle size and dispersion

The particle size and dispersion of a catalyst directly related to its surface area and chemisorptions properties. The particle size can be measured by chemisorptions method [10]. However, the most powerful technique for particle size measurements is the electron microscope. Indeed, particles whose sizes span from the atomic to the macroscopic scale can be directly observed and measured on catalyst images. Techniques based on X-ray diffraction such as line broadening analysis (LBA) [11] and small-angle X-ray scattering (SAXS) [12] are also useful methods since they lead to both mean sizes and size distributions .

c).   Fine structure and chemical properties

The rapid development of electron microscope and X-ray techniques provide the opportunities to carefully study the fine structure, morphology and chemical composition of catalysts. Heterogeneous catalysis being concerned with surfaces, it is recommended in principle that surface sensitive methods should be used. Numerous modern techniques have been applied to characterize fine structures of heterogeneous catalysts. However, this part only lists those which are most commonly used and most related to this dissertation. More detailed description and IUPAC recommendations can be found in the handbook [13].

Electron microscope: The method provides identification of phases and structural information on crystals, direct images of surfaces, and elemental composition and distribution. The most common techniques include: transmission electron microscope (TEM), high resolution transmission electron microscope (HRTEM), scanning electron microscopy (SEM), scanning transmission electron microscopy (STEM) and selected area diffraction (SAD).

X-ray and neutron methods: The X-ray diffraction and absorption can give information of crystalline phases, individual crystal size and elements, which is one of the most important techniques for catalyst characterization. X-ray diffraction (XRD), extended X-ray absorption fine structure (EXAFS) and X-ray absorption near edge structure (XANES) are mostly applied. Along with TEM, energy dispersive X-ray spectroscopy (EDS) can give elemental distribution and semiquantitative analysis.

Neutron diffraction gives the same kind of information as X-ray diffraction, but with larger cross-section between pairs of catalytically important atoms.

Electron spectroscopy: In the form of X-ray photoelectron spectroscopy (XPS), valence band photoelectron spectroscopy (UPS) and Auger electron spectroscopy (AES), the electron spectroscopy has been developed for chemical analysis, which provides information of oxidation state, elemental distribution, and chemical environmental changes. It has advantages of fast data acquisition, small area of sampling, high surface sensitivity and quantitative accuracy. The AES can give spatial distribution information, too.

Secondary ion mass spectroscopy (SIMS): In SIMS a primary ion beam (1–20 keV) causes ejection (sputtering) of neutrals and ions from a solid specimen; the secondary ions are mass-analyzed. The ejected ions and ion clusters give information on the nature and may give clues to the chemical state of species present. With sputtering, the technique gives a depth profile of the sample with a depth resolution of 2–10 nm and a lateral resolution of 1–60 μm.

Vibrational spectroscopy: Though there are many techniques, the mostly used vibrational spectroscopy for solid catalysts is Fourier transform infrared spectroscope (FTIR) and Raman spectroscope. Information is available, either directly or by study of "probe" adsorbates, on the chemical nature of surface groups (particularly on oxides). It is also used for the study of the behavior of precursor compounds during catalyst preparation. Raman is particularly useful in the studies of supported monolayer catalysts and adsorbed layers.

Thermoanalytical techniques: In addition to the techniques mentioned above, thermoanalytical techniques are the most important and widely used methods for the characterization of the properties and reactivities of solid catalysts. These techniques involve the measurements of the response of the solid (e.g. energy or mass released or consumed) as the temperature changed. Most techniques are carried out dynamically by application of a linear temperature program. Differential thermal analysis (DTA), thermogravimetry (TG) and differential scanning calorimetry (DSC) are standard techniques in solid-state chemistry [14]. To understand the gas–solid interactions and the surface reactivities, the techniques of temperature-programmed desorption (TPD), temperature-programmed reduction (TPR) and temperature-programmed oxidation (TPO) have been developed, which typically involve monitoring surface (or bulk) processes between the solid catalyst and its gaseous environment via continuous analysis of the gas-phase composition as the temperature changed. The experiment directly determines the average oxidation state of the solid material and the kinetic parameters [15].

As mentioned above, heterogeneous catalysts have been studied extensively, and have been used in a wide range of industrial fields. In this dissertation, catalysts for hydrocarbons oxidation are particularly studied.

1.2. Catalytic oxidation reaction of hydrocarbons

Hydrocarbons are a primary energy source for current civilizations. The predominant use of hydrocarbons is as a combustible fuel source, which provides more than 80% of the energy nowadays. Catalytic oxidation of hydrocarbons, as an

alternative to conventional thermal combustion, has received considerate attention during the past decades [16-21]. The research efforts have been promoted by the need to meet the required pollutant emissions by the government, and the wish to utilize the fuel more efficiently. The catalytic oxidation process provides two main advantages over the conventional combustion: 1) Catalytic oxidation can occur in a wide range of fuel-to-oxidizer ratio and at low temperatures [22], which is especially beneficial for secondary oxidation of unburned hydrocarbons in emissions; 2) NO_x formation can be eliminated/declined at those low temperatures [23], leading to substantially less NO_x emission. Furthermore, the catalytic oxidation process can provide even temperature distribution and less noise.

However, there are also several issues to address during the catalytic oxidation process. First of all, the stability of the catalysts has been a problem. Aging and poisoning may limit the lifetime of the catalyst and lead to drop in performance. In addition, the introduction of catalysts in reactor causes more complication. It may affect the design of the reactor and generate an extra failure possibility.

Prasad et al. [24] have summarized the requirements for desirable catalysts for hydrocarbons oxidation process:

1. The catalytic activity should be high enough to maintain complete oxidation at the lowest inlet temperature but highest mass supply.

2. The catalysts should be sufficiently stable to be used prolonged at working temperature.

3. The support should have a large specific surface are, good mass and heat transfer and resistance in high working temperature.

Out of all the materials, the noble metals, such as Pt, Pd and Au, are the most active catalysts for the hydrocarbons oxidation process [16, 25]. Apart from the high activity, noble metals are less likely to surfer poisoning and easier to prepare [26]. Pt and Pd are most widely used in catalytic combustion applications, such as in car exhaust catalytic convertors and power plants [27]. However, the limited supply/high cost and high volatility of noble metals urge researches to search for alternative materials for catalytic oxidation of hydrocarbons.

Transition metal oxides have been extensively studies as catalysts for hydrocarbons oxidation [17, 28]. The low cost of raw materials and high thermal stability are the main advantages of metal oxides over noble metals. Studies have also shown that the formation of NO_x can be suppressed over metal oxides [23, 29]. Trimm et. al. [17] proposed that for metal oxides, there is a correlation between the activity and the metal-oxygen bond strength, which is supported by a number of researchers [30-35]. For example, Figure 1.1 shows the rate of propylene oxidation as a function of the heat of formation of the oxide divided by the number of oxygen atoms in the oxide [35]. The heat of formation represents the bond strength. The best catalysts need moderate bond strength, which is good for both the oxidation and reduction of catalysts process. Figure 1.1 shows that the Co_3O_4 and CuO are among the most active metal oxides.
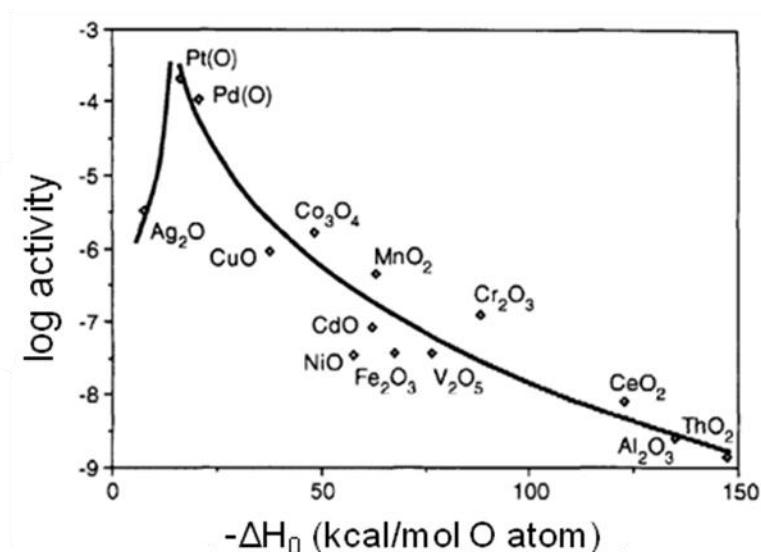
Figure 1.1 Activity of metal oxides in propylene oxidation as a function of the metal-oxygen bond strength. Reproduced from Morooka et. al. [35]. The bond strength is expressed as the heat of formation of the metal-oxygen bond divided by the number of oxygen atoms in metal oxide.

1.3. Previous studies in metal oxide catalysts for hydrocarbons oxidation

1.3.3. Conventional metal oxide nanoparticles (NPs) catalysts

To achieve good performance, large specific surface area and good heat/mass transfer of catalysts is required. Due to the rapid development of nanotechnology these years, catalysts based on nanoparticles (NPs) have been studied and widely used [36-40]. NPs have extremely high surface-to-volume ratio, which benefits a lot in catalytic reactions; porous substrates, such as Al_2O_3 [16, 41-44], ZrO_2 [42, 45, 46] and spinel-type (AB_2O_4) supports [47, 48], are always used as support for metal oxide NPs. This

9

type of supported NPs catalysts have extremely high surface area and are applied in catalytic oxidation of hydrocarbons applications [49].

Nevertheless, the supported NPs have several limitations. First, NPs are susceptible to aggregation at large loadings, causing a reduced catalytic activity. Marion et al. [41] studied the combustion of methane on CuO/Alumina catalysts and the effect of different loadings of Cu. They found that the activity per unit mass of catalyst increases for Cu loading between 2.1% to 4.8%, but then decreases as the Cu loading increases to 9.2% (Figure 1.2). Similar results have been reported by Park and Ledford [43]. They found the activity per unit mass of Cu and per mole of Cu on the surface decrease as the increases of Cu loading. Kundakovic and Flytzani-Stephanopoulos [45] studied the activity of CO and CH_4 oxidation over CuO catalysts supported on stabilized zirconia (YSZ). They found that when Cu loading is 5% to 15%, the metal is highly dispersed as small clusters or isolated atoms, and when Cu loading increases to 40%, bulk CuO begins to form. And according to the authors, the small Cu clusters are more active than the highly dispersed copper species, and bulk CuO contributes little to the catalytic effect. Dongare et al. [46] prepared the Cu-ZrO_2 catalysts by sol-get method and studied the catalytic activity for methane oxidation. They found the most active catalyst corresponds to 20% mole of Cu, which has the maximum amount of copper in the substitutional position. All these study suggested that large loading of NPs catalysts adversely affected the catalytic activity.
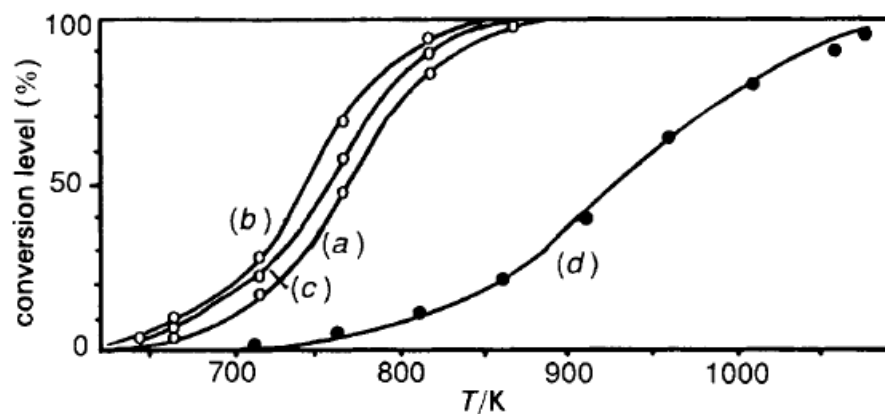
Figure 1.2 Conversion level of methane as a function of the temperature over various CuO/alumina catalysts: (a) 2.1 wt % CuO/alumina (fresh state); (b) 4.8 wt % CuO/alumina (fresh state); (c) 9.2 wt % CuO/alumina (fresh state); (d) 4.8 wt% CuO/alumina (aged state: 9 vol % methane in air). Reproduced from Marion et al. [41].

Secondly, the supports can impact the activity of the metal oxide NPs, which increase the complication of the fundamental study of the inert catalytic properties of the metal oxides themselves. For example, Aguila et al. [42] studied the CuO catalysts supported on ZrO_2, Al_2O_3 and SiO_2 with different metal concentration on the activity of methane oxidation. They found that the activity of the catalysts, per mass of loaded Cu, follows the sequence: $CuO/ZrO_2 > CuO/Al_2O_3 >> CuO/SiO_2$. Similar results have been shown for other metal oxides. In addition, solid-state reactions between NPs and the supports may occur at high temperature and the catalytic activity will decrease [41]. The interactions between NPs and supports complicate the fundamental study of the NP catalysts, and also require careful choices of supports.

Finally, preparation of supported NPs can be tedious, typically including co-precipitation, purification and calcinations [50-52]. The above results indicate that there is demand to develop alternative forms of metal oxide catalysts to NPs.

1.3.4. 1-D metal oxide nanostructures for hydrocarbons oxidation

Compared with NPs, one-dimensional (1-D) nanostructures, such as nanorods [53-58], nanowires [59-61] and nanotubes [62, 63], have large surface-to-volume ratios, are more stable and always have some particular growth directions, which gives rise to higher catalytic activity. More and more study has been done in 1-D nanostructured materials in catalytic reactions recently [64].

1-D nanostructured materials are used both as supports for the noble metals and as catalysts directly. For example, in catalytic oxidation of CO and hydrocarbons, 1-D nanostructured materials supports can improve the catalytic activity of the noble metals. Huang et al. [53] studied the catalytic activity of Au nanoclusters deposited on a 1-D CeO_2 nanorods and CeO_2 nanoparticles during CO oxidation at ambient temperatures. The kinetic data showed that the activity of Au catalysts could be remarkably improved by using CeO_2 nanorods as support compared to the CeO_2 nanoparticles. In Maiyalagan and Viswanathan's study [55], WO_3 nanorods are served as supports for Pt nanoparticles and a film of Pt/WO_3 nanorods on a glassy carbon electrode exhibits good electrocatalytic activity towards the oxidation of methanol.

There are several examples that 1-D nanostructured materials are served as catalysts directly and have shown some promising results [54, 56, 58, 59, 61, 62, 65]. Xie et al. [56] invested the low-temperature oxidation of CO over Co_3O_4 nanorods.

12

They reported the catalysts not only catalyze CO oxidation at temperatures as low as -77 ^{o}C but also remain stable in a moist stream of normal feed gas for more than 60 hours (Figure 1.3). They proposed the significantly higher reaction rate due to predominant exposed [110] planes of Co_3O_4 nanorods, favoring the presence of active Co^{3+} species at the surface. Gonzalez-Rovira et al. [62] studied the catalytic activity of CeO_2 nanotubes for the CO oxidation and compared with that of polycrystalline powder CeO_2 sample. The activity of the CeO_2 nanotube is shown to be in the order of 400 times higher per gram of oxide at 200 degrees C than the powder CeO_2. They explained this highly improved performance for several reasons. At first, the nanotubes are built by assembling a huge number of randomly oriented small nanocrystals, giving rise to a significant volume of very reactive boundary regions between the nanocrystals, where the catalytic reaction occurs most actively. Likewise, a greater contribution of the more reactive [66] facets to the surface structure of the material may also contribute to the observed catalytic performance enhancement. Similar comparison between NWs and NPs has been done on carbonates for ethanol degradation as well [61]. Wang and Zhu found $SrCO_3$ nanowires have lower ignition temperatures and wider working temperature ranges than NPs, though NWs had lower surface areas. They attributed the differences in catalytic degradation activity between $SrCO_3$ NWs and NPs to different distributions of active sites on the surfaces.
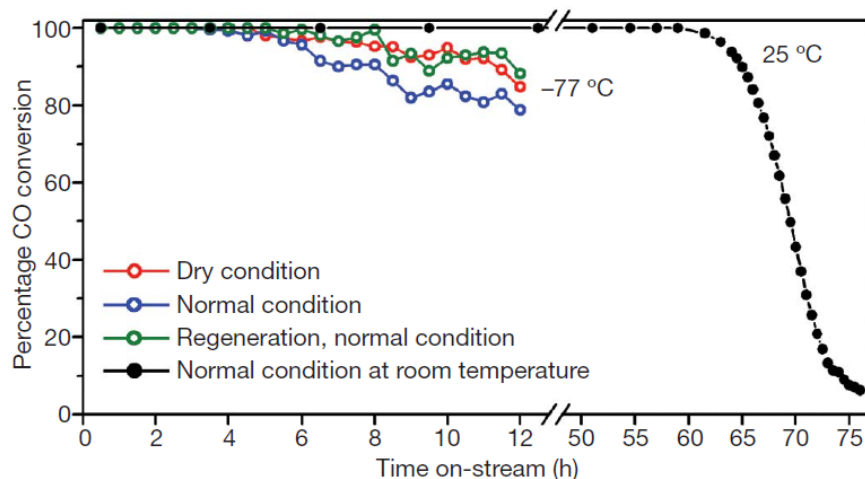
Figure 1.3 The oxidation of CO over Co_3O_4 nanorods. CO oxidation with a feed gas of 1.0 vol.% CO/2.5 vol.% O_2/He under normal (moisture 3–10 p.p.m., blue symbols) and dry (moisture ,1 p.p.m., red symbols) conditions at 277°C. The used sample was regenerated with a 20 vol.% O2/He mixture at 450 ^{o}C for 30 min and then tested for CO oxidation under normal conditions (green symbols) at 277°C. CO oxidation at 25 ^{o}C (black symbols) was tested with the normal feed gas. Reproduced from Xie et. al. [56].

Although the study on 1-D metal oxide catalysts is limited, the previous study has demonstrated that 1-D nanostructured metal oxides are promising candidate for catalysts due to their facet structures, small grains and stable naure.

1.4. Objectives

The primary objective of this dissertation is to study the catalytic properties of the 1-D nanostructured metal oxides for hydrocarbons oxidation, and to exhibit the 1-D catalysts is an alternative to the supported NPs catalysts. Particularly, to further

simplify the system and take morphology merits of the 1-D structure, we focus on the metal oxide NWs on metal mesh substrates.

This morphology has many benefits. Firstly, the NWs grow on the metal mesh substrates, so that the NWs adhere strongly to the substrates. As a result, the NWs can avoid aggregation even at high number density. In this way, the catalytic activity can be increased by simply increasing the loading of the NWs. Secondly, the metal oxide NWs is the only oxide in the system, which eliminates the reactions between active materials and supports, leading to good stability and a clean system for fundamental study. More importantly, the surface of NWs is exposed, instead of embedding in supports, which enables easy surface treatment and decoration for further enhancement of catalytic activity. In addition, the flexible opening in metal mesh supports provides good heat and mass transfer [67, 68].

By examining Figure 1.1, Co_3O_4 and CuO were chosen as the catalysts to study in this work, due to their highest activity among all the metal oxides, and their simplicity to grow as NWs on metal mesh supports. Although CuO has been extensively studied for hydrocarbons oxidation, the CuO NWs as catalysts, to our best knowledge, have not been investigated. Moreover, the direct comparison of NWs and supported NPs is limited. Thus, the first objective of this thesis is to study the CuO NWs for catalytic oxidation of hydrocarbons, and compare its activity to that of bulk CuO and supported CuO NPs.

The decoration and modification of catalysts is difficult for the supported NPs for their geometric nature. However, it is easy to achieve on NWs. Thus, to exhibit the

15

morphology merits and explore the potential of the NWs, this thesis also studies the modification and decoration of NWs for further enhancement in catalytic activity.

Finally, Co_3O_4 is known to be the most active metal oxide for catalyzing hydrocarbons oxidation. However, the growth of Co_3O_4 NWs on metal mesh has not been well developed. On the other hand, the synergetic effect of Cu and Co is also attractive. Thus, the third objective of this thesis is to study the growth of Co_3O_4 NWs and the synergetic effect between Cu and Co in catalytic reaction.

1.5.   Scope of the dissertation

The main body of the dissertation includes 7 chapters.

Chapter 1 introduces the backgrounds of the catalysts, catalytic oxidation of hydrocarbons and the previous studies of the metal oxide catalysts by reviewing the current literature and the objectives of this work.

Chapter 2 to 5 elaborates on the research by the author in the 1-D nanostructured metal oxide catalysts for hydrocarbons oxidation.

Chapter 2 examines the copper oxide (CuO) NWs, as a model system, to show the catalytic properties of 1-D nanostructured metal oxide. First, the CuO NWs were grown on Cu substrates with the thermal annealing method, and were characterized by various techniques. The catalytic activity of CuO NWs was examined for methane oxidation, and further compared to that of the supported CuO NPs and the bulk CuO. In addition, the catalytic mechanism and reaction kinetics were also analyzed.

Since the surface of the NWs is exposed, it is easy to further modify in order to enhance the catalytic activity. In Chapter 3 and 4, two methods were used to treat the CuO NWs to increase its catalytic activity.

In Chapter 3, a radio frequency (RF) plasma was applied to treat the CuO NWs to modify both the physical and chemical properties of the CuO NWs. The plasma treatment effects were examined by characterizing the materials and catalyzing CO oxidation. The catalytic mechanism and reaction kinetics was studied. Particularly, the Cu (I) and Cu (II) in catalytic reaction was compared and the reasons for more active Cu (I) were also investigated.

Chapter 4 introduced a newly developed sol-flame method, which was applied to decorate CuO NWs with more active Co_3O_4 NPs for further enhancement of the catalytic activity. The Co_3O_4 NPs decorated CuO NWs were used as catalyst for methane oxidation, and their activity was compared to bare CuO NWs and CuO NWs decorated by other methods.

In addition, the sol-flame method was found to be a general method to synthesize hybrid NWs, including NP decorated NWs, core/shell NWs and doped NWs. Various hybrid NWs were synthesized by sol-flame method and thoroughly characterized in Chapter 5. The experimental parameters effects were examined and other potential applications were discussed.

In addition to physically bonding Co_3O_4 and CuO, another way to study their synergetic effects is to grow both of them in-situ. In Chapter 6, 1-D structured Co_3O_4 was grown by hydrothermal method with adding Cu in the solution. The effect of Cu addition was investigated, and the growth mechanism was proposed. The catalytic

17

activity of the $Co_3O_4\_Cu$ structures was analyzed by catalyzing methane oxidation, and the synergetic effect of Co and Cu was also studied.

Finally, Chapter 7 summarized the research the author has done and presents some future research possibilities.

Chapter 2.   CH$_4$ Oxidation over Catalytic CuO NWs

2.1.   Introduction

Since the foremost objective of this thesis is to investigate the catalytic properties of metal oxide NWs for hydrocarbons oxidation, and compare that to supported NPs, the copper oxide (CuO) is a good system to start with, for its relatively high activity, easiness to grow as NWs, and abundant previous study.

Extensive study has been done on CuO NPs supported on porous substrates, such as Al$_2$O$_3$ [42, 43, 69], ZrO$_2$ [42, 45], CeO$_2$ [51, 52, 70-74] and spinel-type (AB$_2$O$_4$) supports [48]. Marion et al. [69] studied the oxidation of CH$_4$ on CuO/Alumina with loadings between 2.1 and 9.2 wt% CuO. They found that the alumina-supported CuO is more active than bulk CuO, but that the catalytic activity decreases with increasing loading of CuO. Similar results were reported by Park and Ledford [43], who found that the ratio of isolated/interacting copper surface phases decreases with increasing Cu content and proposed that the isolated Cu surface phase is more active for CH$_4$ oxidation than the interacting Cu surface phase or crystalline CuO. Aguila et al. [42] recently reported that the catalytic activity for CH$_4$ oxidation, per gram of loaded Cu, follows the sequence: CuO/ZrO$_2$ > CuO/Al$_2$O$_3$ >> CuO/SiO$_2$, indicating a strong influence from the supports. Although the catalytic activity of supported CuO NPs is reasonably high, there are several limitations. First, interactions between the support and NPs at high temperatures [69] impede the fundamental understanding of the catalytic properties of individual NPs, and limit their application conditions. Moreover,

19

the solid supports limit the loading of NPs because NPs tend to aggregate at large loadings, leading to a decrease in catalytic activity [42, 43, 69].

Methane (CH_4) was used as fuel in this study, for it is the main component of natural gas and a key intermediate in hydrocarbon oxidation. Herein, we studied the catalytic oxidation of CH_4 over CuO NWs to explore the fundamental catalytic properties and practical merits of these 1-D nanocatalysts. The CuO NWs were synthesized by thermal annealing. The effects of the CuO NW loading, copper oxidation states and stability were investigated, and their catalytic activities, in terms of reaction rates, were compared with those of supported CuO NPs and bulk CuO. The results strongly suggest that CuO NWs are promising catalysts because of their relatively high catalytic activity, stability, low cost and flexibility.

2.2. Experimental Specifications

2.2.1. Synthesis of CuO NWs

CuO NWs can be prepared by a number of methods, including hydrothermal decomposition [75], self-catalytic growth [76], solvothermal process [77], flame synthesis [78] and thermal annealing [79]. We adopted the thermal annealing method because it is simple, economical and can conveniently tune the length, diameter and density of the CuO NWs by the variations of the annealing temperature and time [80, 81]. Briefly, a piece of copper mesh (mesh density: 100×100 per square inch, wire diameter: 0.0045", McMaster) with dimensions of 3" $\times 12$" was rolled up to a 3" long

cylinder (Figure 2.1a) and annealed in a tube furnace at 520°C for two days, unless otherwise specified.
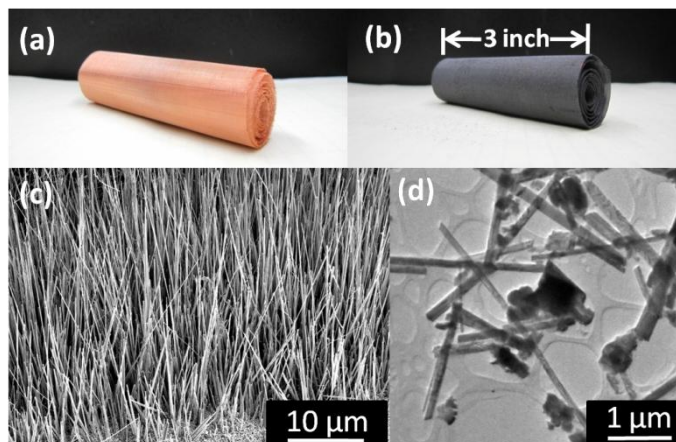
Figure 2.1 Photographs of (a) the copper mesh and (b) the annealed copper mesh (520°C, two days) with the as-grown CuO NWs. (c) SEM image and (d) TEM image of the as-grown CuO NWs. The average length and diameter of CuO NWs are 50 μm and 100 nm.

2.2.2. *Material characterization of CuO NWs*

After the copper mesh was annealed at 520°C for two days, its color changed from bright yellow to black (Figure 2.1a and b), indicating that Cu was oxidized to CuO. The morphology, crystal structure, composition, and oxidation state of the as-grown CuO NWs were further examined by scanning electron microscopy (SEM, FEI XL30 Sirion, 5kV), transmission electron microscopy (TEM, FEI Tecnai G2 F20 X-TWIN FEG, 200 kV), and X-ray photoelectron spectroscopy (XPS, SSI S-Probe Monochromatized, Al kα radiation at 1486 eV, 150 × 800 μm spot). The SEM and

TEM images in Figure 2.1c and d show that the CuO NWs were formed perpendicularly to the copper mesh with an average diameter of 100 nm and length of 50 μm, and an estimated coverage density of 10^8 NWs/cm^2. The specific surface area of the catalyst was estimated to be about 0.08 m^2/g [66], which is smaller than those of the typical supported CuO NPs (36 ~ 208 m^2/g) [42], because the major mass of the catalytic CuO NWs comes from the copper mesh and the surface oxide layers.

2.2.3. *Measurement of the catalytic activity of CuO NWs*

The catalytic activity of the CuO NWs for CH$_4$ oxidation was measured in an in-house built tube flow reactor. As shown in Figure 2.2, the reactor consists of a quartz tube (90 cm long, 2 cm inner diameter) housed in a tube furnace. The inflow was a mixture of 1.5 vol.% CH$_4$ and 6 vol.% O$_2$ diluted with helium, with a total flow rate of 100 sccm, unless otherwise specified. The flow rate of each gas was controlled by mass flow controllers (MFC, Z500, Horiba). The effluent gas was connected to a gas chromatograph (GC, SRI Multiple Gas Analyzer) directly for composition analysis. The CH$_4$ conversion percentage is defined as

$$CH_4\% = \frac{X_{CH_4}(\text{initial}) - X_{CH_4}(\text{effluent})}{X_{CH_4}(\text{initial})}$$

(2.1)

, where X_{CH4}(initial) and X_{CH4}(effluent) are the CH$_4$ mole fractions in the inflowing and effluent streams, respectively. For each experimental condition, the effluent gas was sampled for composition analysis every 15 minutes for 45 minutes and the repeatability of the CH$_4$ conversion percentage was within $\pm 2\%$ of the average value.
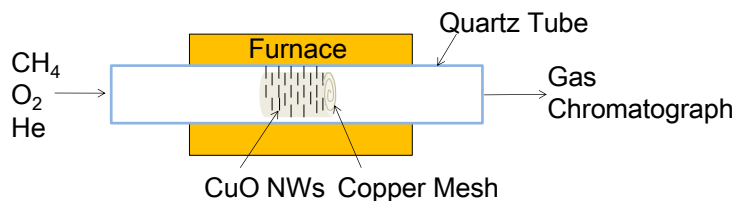
Figure 2.2 Schematic diagram of the in-house built tube flow reactor for the catalytic activity test.

2.3. Results and Discussion

2.3.4. Catalytic oxidation of CH_4 over CuO NWs

The effect of the synthesis conditions of the CuO NWs on their catalytic activities is illustrated in Figure 2.3, where the CH_4 conversion percentage over CuO NWs grown for different durations is plotted as a function of temperature. First, the CuO NWs grown for two hours and two days both greatly facilitate the CH_4 oxidation process, because the CH_4 conversion percentage is almost zero without any catalyst at 500^oC. Second, the CH_4 conversion percentage increases with increasing the length and surface coverage density of the CuO NWs. The SEM images in Figure 2.3 insets show that the length and coverage density of NWs grown for two days are much larger than those of NWs grown for two hours, and, correspondingly, the CH_4 conversion percentage is increased from 14% to 38% at 500^oC. In both cases, the copper meshes have the same dimensions with the same surface area of CuO layers, so it is the CuO NWs, not the surface CuO layer, that play a significant role in the catalytic process. In

23

other words, the increase in the CH_4 conversion percentage comes from the increased loading of the CuO NWs.
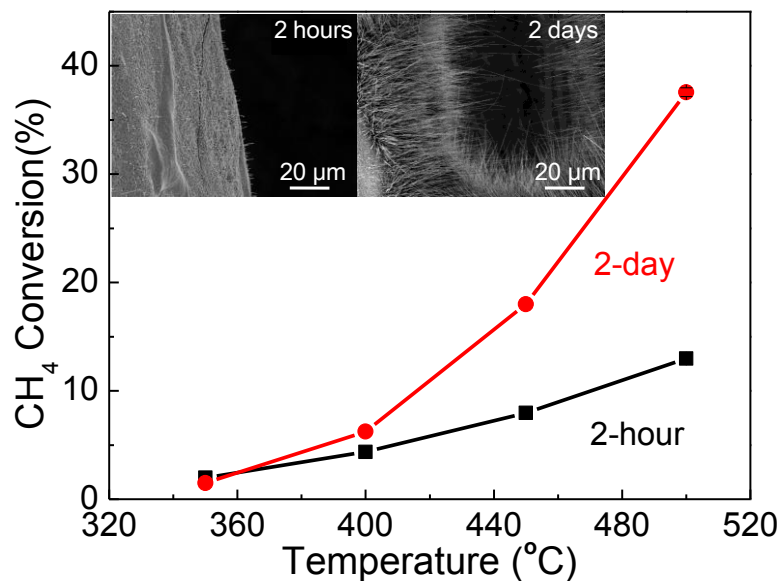
Figure 2.3 CH_4 conversion percentage versus temperature over catalytic CuO NWs grown for different durations. Insets: SEM images of CuO NWs grown for two hours (left) and two days (right) of annealing at 520^oC.

The effect of CuO NW loading was further investigated by varying the size of the copper meshes. CuO NWs were grown at 520^oC for two days on four pieces of copper mesh with sizes of 3" $\times$ 4", 3" $\times$ 8", 3" $\times$ 10" and 3" $\times$ 12", which were all rolled up into 3" long cylinders. The catalytic activity of these four different CuO NW loadings was tested for CH_4 oxidation at 400^oC, 450^oC and 500^oC, respectively. As shown in Figure 2.4, at all the temperatures, the CH_4 conversion percentage increases with the loading of CuO NWs monotonically and gradually levels off. Because of the simple

geometry of the copper meshes, the loading of CuO NWs can be easily increased by rolling more copper meshes per unit volume, without increasing the size of the catalytic reactor.
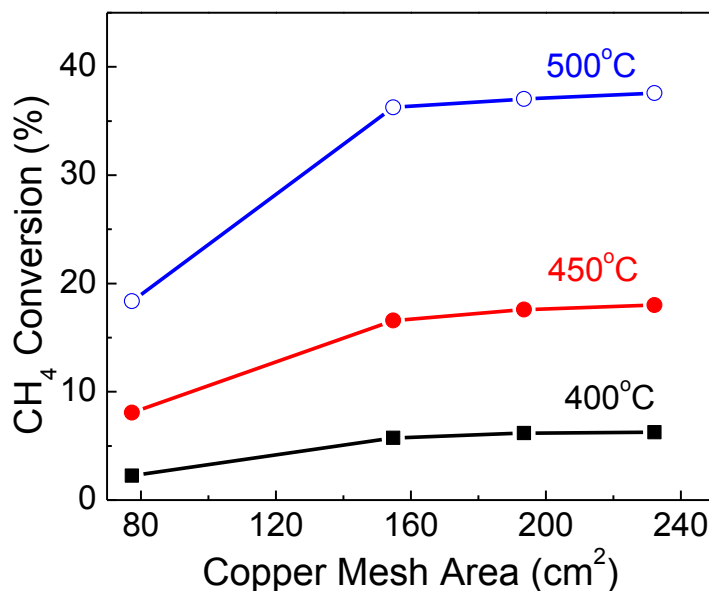
Figure 2.4 CH$_4$ conversion percentage versus catalytic CuO NWs loading at 400 ^{o}C, 450°C and 500°C.

The catalytic stability of the as-grown CuO NWs was tested at 500°C. The CH$_4$ conversion percentage is plotted vs. time in Figure 2.5. The CH$_4$ conversion percentage remains fairly constant, at 38.95 ± 1.53%, over the 24-hour testing period. More importantly, after the CuO NWs were completely removed from the copper mesh by sonication, new CuO NWs were grown when the same copper mesh was annealed again at 520°C for two days. The regenerated CuO NWs have catalytic activity and stability comparable to those of the original NWs, as evidenced by the

near 40% CH_4 conversion percentage for more than 24 hours (Figure 2.5). The capability of regenerating CuO NWs *in situ* with comparable catalytic activity and stability is a unique advantage that is not shared by conventional catalysts.
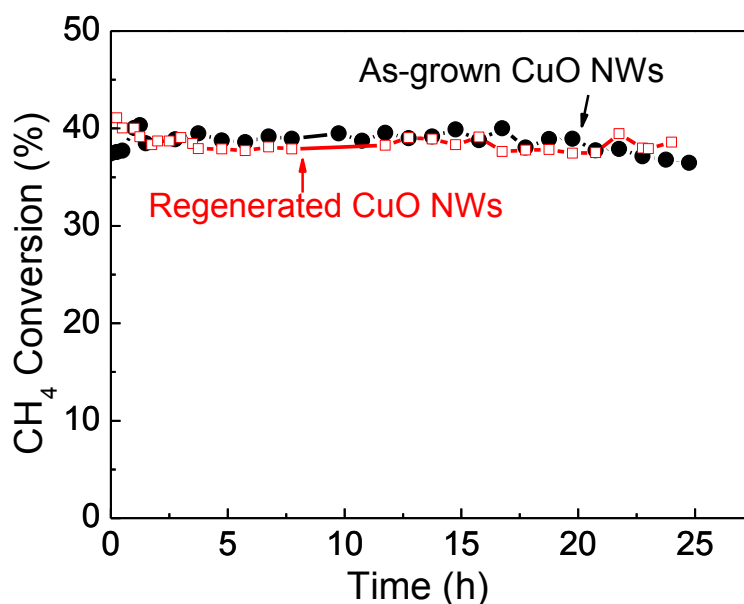
Figure 2.5 CH_4 conversion percentage versus time at 500°C over the as-grown and the *in situ* regenerated CuO NWs.

2.3.5. *Analysis of chemical kinetics*

Since the convection time scale is much shorter than those of the chemical reactions in our experiments, chemical reaction is the rate limiting process for the conversion of CH_4. Oxidation reactions over oxide catalysts, such as CH_4 oxidation over CuO, are generally agreed to follow a Mars-van Krevelen redox mechanism [82, 83]:

$$R + xO\text{-}S \xrightarrow{k_1} P + xS \tag{R2.1}$$

$$(x/2)[2S + O_2 \xrightarrow{k_2} 2O\text{-}S] \tag{R2.2}$$

, where R, O-S, S and P represent the reactant, a surface active site covered by oxygen, a surface active site without oxygen and products, respectively. Assuming that R2.1 is first order with respect to R and O-S and that the reaction rate of surface oxygen adsorption (R2.2) is proportional to $P_{O_2}^n$, where P_{O_2} is the partial pressure of oxygen, the consumption rate of R can be expressed as

$$r_R = k_1 p_R \theta \tag{2.2}$$

, where θ is the concentration of O-S and p_R is the partial pressure of the reactant. At steady state, it can be shown [30] that

$$\theta = \frac{k_2 p_{O_2}^n}{(x/2)k_1 p_R + k_2 p_{O_2}^n} \tag{2.3}$$

$$r_R = \frac{k_1 k_2 p_R p_{O_2}^n}{(x/2)k_1 p_R + k_2 p_{O_2}^n} \tag{2.4}$$

When the reaction rate coefficients for R2.1 and R2.2 are significantly different, r_R can be simplified as follows:

$$\text{when } k_1 \gg k_2, \quad r_R = k_2 p_{O_2}^n \tag{2.5}$$

$$\text{when } k_1 \ll k_2, \quad r_R = k_1 p_R \tag{2.6}$$

To further identify the rate determining step, we measured the CH_4 conversion rate under different concentrations of CH_4 and O_2 in the inflowing stream. The fitted reaction orders of CH_4 and O_2 over the as-grown CuO NWs were 0.93 and 0.20 at

27

500°C (Figure 2.6a), respectively, suggesting that the NW surfaces are almost saturated with O_2, leading to a weak dependence of the reaction rate on the gas phase O_2 concentration. In contrast, the CH_4 conversion rate is almost linearly proportional to the concentration of CH_4, in agreement with Eq. (2.6), so the first global reaction, R2.1, is probably the slower or rate determining step. Since R2.1 includes several elementary reactions, i.e., the adsorption of CH_4 on the active surface sites, the oxidation of CH_4, and the desorption of the products, more investigation is needed to the identify the rate determining elementary step, though some studies suggested that it is the cleavage of the C-H bond [43].
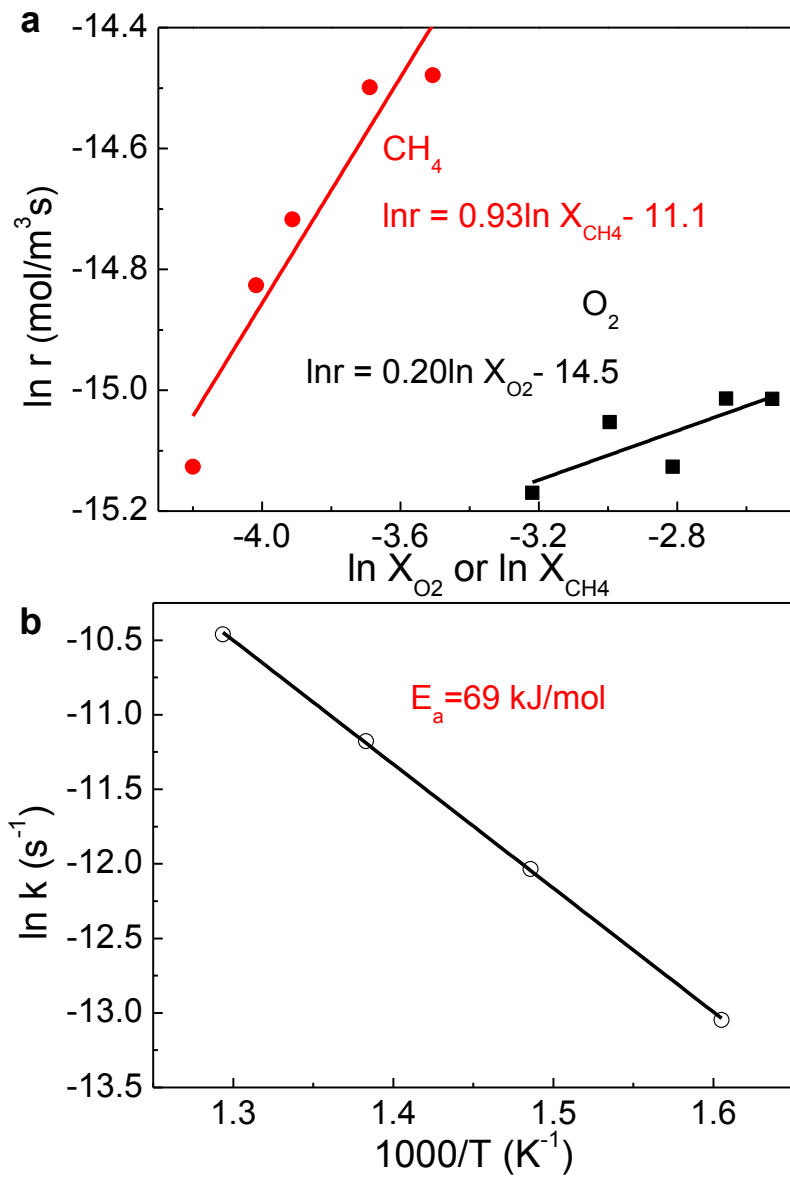
Figure 2.6 (a) Reaction rate of CH_4 oxidation over the as-grown CuO NWs at 500°C as functions of the mole fractions of CH_4 and O_2 (X_{CH_4} and X_{O_2}). (b) Arrhenius plot of the reaction rate coefficients of CH_4 oxidation over the as-grown CuO NWs versus temperature. The inflow is 1.5 vol.% CH_4 and 6.0 vol.% O_2 diluted in helium.

The reaction rate coefficients k_1 were subsequently calculated from concentration measurements over a temperature range of $350^{\circ}C$ to $500^{\circ}C$ using Eq. (2.6), and the overall activation energy of CH_4 oxidation over the as-grown CuO NWs was extracted to be 69 kJ/mol (Figure 2.6b), which is smaller than that of CH_4 oxidation over supported CuO NPs, 96 kJ/mol [42], suggesting that NWs might be more effective than supported NPs.

2.3.6. Comparison of catalytic activity of CuO NWs with bulk CuO and supported CuO NPs

We further compared the catalytic activity of CuO NWs with bulk CuO and supported CuO NPs to evaluate the potential of CuO NWs. The catalytic activity is defined in terms of the reaction rate, which is calculated as the ratio of the measured CH_4 conversion rate to the mass or surface area of the catalyst used:

$$r = \frac{\text{Molar flow rate of } CH_4 \times \text{Conversion percentage of } CH_4}{\text{Mass (or surface area) of catalyst}} \left[\frac{mol}{g \cdot s} \left(\text{or } \frac{mol}{m^2 \cdot s} \right) \right]$$

(2.7)

To accommodate the differences in the catalytic structures and copper oxidation states reported in the literatures, we calculated separate reaction rates, each based on one of three different characteristics of the catalyst: (1) r_{am}, based on the mass of Cu in the active catalyst, excluding that in the supporting substrate (for CuO NWs, we only count the Cu mass in the NWs [84]); (2) r_{ts}, based on the total surface area of the catalyst, including supporting substrates; and (3) r_{as}, based on the surface area of the active catalyst, excluding that of the supporting substrate (i.e., surface area of the CuO

NPs for supported CuO, surface areas of NWs only). The resulting reaction rates for the CuO NWs, supported CuO/ZrO_2 [42] and bulk CuO [69] at $400\,^\circ$C and 500°C are summarized in Table 2.1. First, the reaction rates (r_{am}) of the CuO NWs are several times larger than that of bulk CuO because the NWs have larger surface-to-volume ratios than the bulk. Second, the reaction rates based on the total surface area of catalysts (r_{ts}) for the NWs are almost one order of magnitude larger than that of the supported CuO NPs. One major reason is that only a small percentage of the supporting ZrO_2 substrate area is occupied by CuO NPs, while the surface coverage density of CuO NWs on the Cu mesh is very high. Therefore, the supporting substrate is more effectively utilized by the NWs. The reaction rate per unit surface area of CuO (r_{as}) is likely the best indicator of the catalytic activity per surface site. Although the reaction rates for the NWs (r_{as}) are smaller than that of 1.3% CuO/ZrO_2, one of the best cases reported, they are still larger than that of 9% CuO/ZrO_2. Overall, the comparison indicates that the catalytic activities of the CuO NWs for CH_4 oxidation are better than that of bulk CuO and comparable to that of supported NPs.

Table 2.1 Reaction rates for CuO NWs, supported CuO NPs and bulk CuO catalysts.

Catalyst	Reaction rate per unit mass of Cu[a] (mol /g s) $\times$ 10^5 (r_{am})		Reaction rate per unit surface area of catalyst[b] (mol /m^2 s) $\times$ 10^8 (r_{ts})		Reaction rate per unit surface area of CuO[a] (mol /m^2 s) $\times$ 10^8 (r_{as})	
	$400\,^\circ$C	$500\,^\circ$C	$400\,^\circ$C	500°C	$400\,^\circ$C	$500\,^\circ$C
CuO NWs	0.06	0.34	6.98	41.93	6.98	41.93
1.3% CuO/ZrO_2 [42]	—	—	0.69	6.20	19.17	172.20

9% CuO/ZrO$_2$ [42]	—	—	0.82	6.91	3.29	27.75
Bulk CuO [69]	0.02	0.18	—	—	—	—

[a] CuO (or Cu) includes the active catalytic part only. For catalytic CuO NWs, it means the CuO NWs (or Cu in CuO NWs). For CuO/ZrO$_2$, it means the CuO NPs.

[b] Catalyst includes the CuO and the supporting substrates (ZrO$_2$ or copper mesh).

2.4. Conclusion

In summary, we have demonstrated that the CuO NWs are promising catalysts for CH$_4$ oxidation due to their simplicity and low cost in synthesis, notable stability in operation, suitability for *in situ* regeneration, flexibility in loading variation, and most importantly, comparable catalytic activities to those of supported CuO NPs. Our kinetic analysis shows that the oxidation rate of CH$_4$ has a nearly linear dependence on the CH$_4$ concentration but a weak dependence on the O$_2$ concentration, so the oxidation step of CH$_4$ by the surface oxygen is likely to be the rate determining step.

Chapter 3.   Plasma-Enhanced Catalytic CuO NWs for CO Oxidation

3.1.   Introduction

In Chapter 2, CuO NWs were studied for catalyzing methane oxidation, and compared to supported NPs and bulk CuO. The results have shown that CuO NWs are promising catalysts. First, CuO NWs can be directly synthesized on copper substrates [79], and there is no chemical interaction between the CuO NWs and the top CuO layer of the Cu substrate. Hence, the configuration of CuO NWs provides a simplified platform to study the fundamental catalytic properties of CuO. Second, loading of CuO NWs can be increased by increasing the density and length of CuO NWs without aggregation [85]. Finally, the CuO NWs have good stability and can be in-situ regenerated.

To take advantage of the exposed surface of NWs, here, we treat CuO NWs with non-equilibrium radio frequency (RF) plasma treatment. Previous studies have shown that RF plasma can change the chemical composition and structure of catalysts and increase their surface area, and hence improve their catalytic activity [86]. Specifically, we have investigated the CO oxidation over the as_grown, argon (Ar) and hydrogen (H_2) plasma-treated CuO NWs, and studied the mechanism responsible for the plasma enhancement effect.

3.2.   Experimental Specification

The CuO NWs were grown by the thermal annealing method [79] (noted as CuO_as_grown) and described in detail in Chapter 2. The CuO_as_grown NWs were further treated by a non-equilibrium RF plasma (Advanced Energy, RFX-600, 13.6 MHz), which was operated at 200 W and 2.5 Torr with either an Ar or H_2 flow rate of 10 sccm for 20 minutes (notated as CuO_Ar_RF and CuO_H$_2$_RF for the Ar and H_2 plasma treated CuO NWs, respectively). The CuO_as_grown, CuO_Ar_RF and CuO_H$_2$_RF NWs were examined using a scanning electron microscope (SEM, FEI XL30 Sirion, 5kV). As shown in Figure 3.1a, the CuO_as_grown NWs are formed perpendicularly to the copper mesh with a diameter range of 100 - 200 nm and an average length of 50 μm, and an estimated coverage density of 10^8 NWs/cm [79, 81, 87]. The CuO_Ar_RF NWs (Figure 3.1b) and CuO_H$_2$_RF NWs (Figure 3.1c) have similar diameters, lengths, and densities as those of the CuO_as_grown NWs, but several of the CuO_Ar_RF NWs become curly, and almost all the CuO_H$_2$_RF NWs are curved. Transmission electron microscope (TEM, FEI Tecnai G2 F20 X-TWIN FEG, 200 kV) images show that the CuO_as_grown NWs (Figure 3.1d and g) are in good crystalline, while the CuO_Ar_RF NWs (Figure 3.1e and h) and CuO_H$_2$_RF NWs (Figure 3.1f and i) have many grain boundaries with an average grain size of 10 nm. These grain boundaries are formed because of the physical impact of electrons and ions from the plasma and the extraction of oxygen, creating strains in the crystal, and the relaxation of the strains along the NWs radial direction causes the NWs to bend.
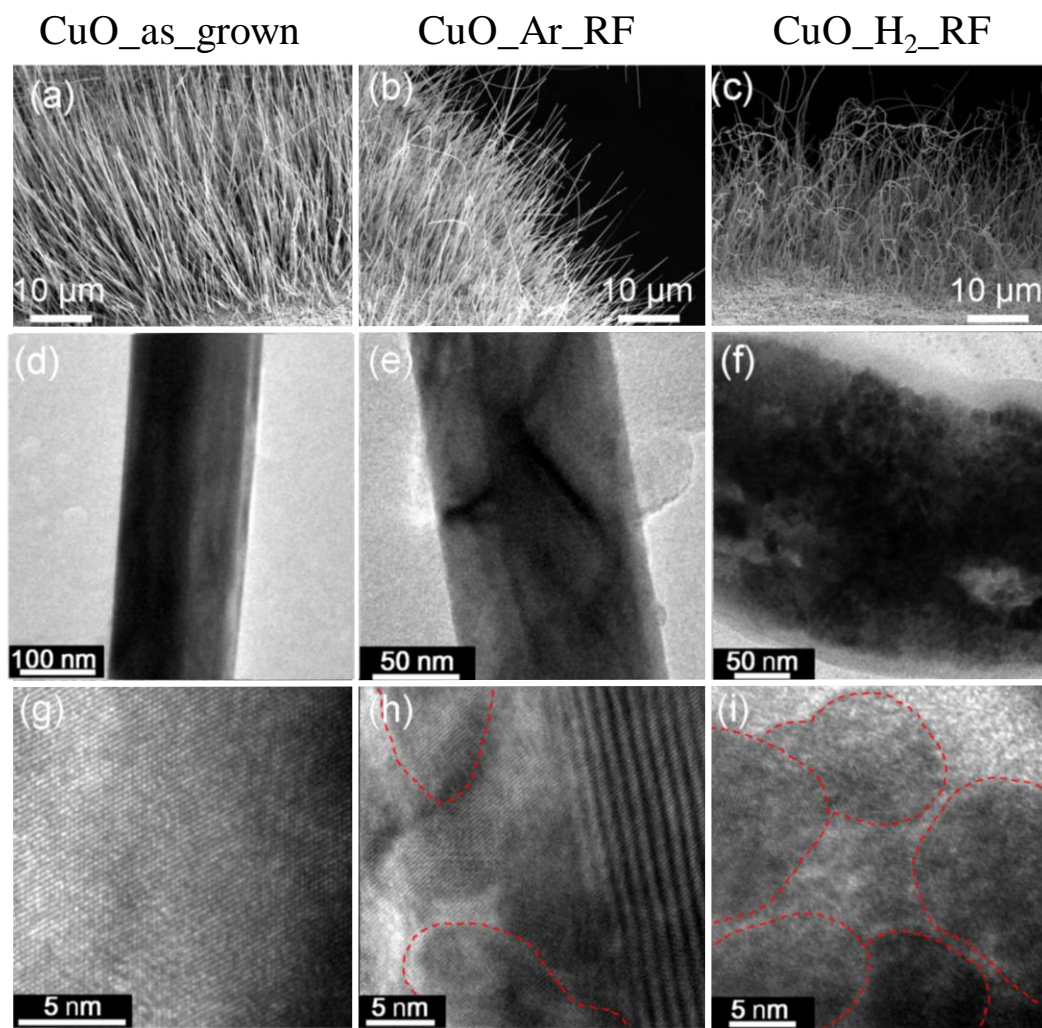
Figure 3.1 SEM, TEM and HRTEM images of the CuO_as_grown (a, d and g), CuO_Ar_RF (b, e and h), and CuO_H$_2$_RF (c, f and i) NWs.

The catalytic activity of the above three types of CuO NWs for the oxidation of CO was measured in an in-house built tube flow reactor. The inflow was a mixture of 2.0 vol.% CO and 3.0 vol.% O$_2$ for the fuel-lean case (equivalence ratio $\Phi = 0.33$), and 2.0 vol.% CO and 0.7 vol.% O$_2$ for the fuel-rich case ($\Phi = 1.43$), and both mixtures were balanced in helium (He), with a total flow rate of 300 sccm. The flow rate of

each inflow gas was controlled by mass flow controllers (MFC, Z500, Horiba). The composition of the effluent gas was analyzed using a gas chromatograph (GC, SRI Multiple Gas Analyzer). The CO conversion percentage is calculated by

$$CO\% = \frac{X_{CO_2}}{X_{CO_2} + X_{CO}} \times 100\% \tag{3.1}$$

, where X_{CO_2} and X_{CO} are the molar percentages of CO_2 and CO in the effluent gas, which were determined from the integrated peak areas of the CO_2 and CO peaks detected by GC. The error of the CO% was within $\pm 2\%$. All the experiments were carried out at 140^oC and 1 atm, unless specified.

3.3.   Results and Discussion

3.3.1. Plasma effects on catalytic activity for CO oxidation

Figure 3.2a and b compare the CO conversion percentage as a function of time over the CuO_as_grown, CuO_Ar_RF and CuO_H$_2$_RF NWs under the fuel-lean and fuel-rich conditions. For the initial several hours, the CO conversion percentage varies slightly over the CuO_as_grown and CuO_Ar_RF NWs, but increases dramatically over the CuO_H$_2$_RF NWs in both lean and rich cases, probably due to the reorganization of the catalyst surface. After the initial stabilization, it can be seen that, for both the fuel-lean and rich cases, the catalytic activity increases in the order of the CuO_as_grown, CuO_Ar_RF, and CuO_H$_2$_RF NWs, with the last one being much

higher. It should be noticed that in the fuel-rich condition, the three CuO NWs act as oxidizers as well due to the insufficient amount of gaseous O_2, so the conversion percentage of CO can be over 80%. These observations are consistent with our previous study on CH_4 oxidation [85] in that RF plasma treatment can enhance the catalytic activity of CuO NWs. There are two major reasons for the enhancement. One is that plasma treatment generates many grain boundaries (Figure 3.1h and i), where reactions occur most easily, so the activity of the two plasma treated NWs is higher than that of the CuO_as_grown NWs. More importantly, plasma treatment, particularly H_2 plasma treatment, reduces Cu(II) to a lower oxidation state Cu(I), according to the X-ray photoelectron spectroscopy (XPS, SSI S-Probe Monochromatized, Al Kα radiation at 1486 eV, 150 $\times$ 800 μm spot) analysis shown in Figure 3.2d. Cu(I) has been shown to be more active than Cu(II) in catalyzing the oxidation of CO [87-91]. It should be noted that RF plasma enables H_2 reduction to occur at lower temperature [92] than thermal reduction, which helps to sustain the NW structure.
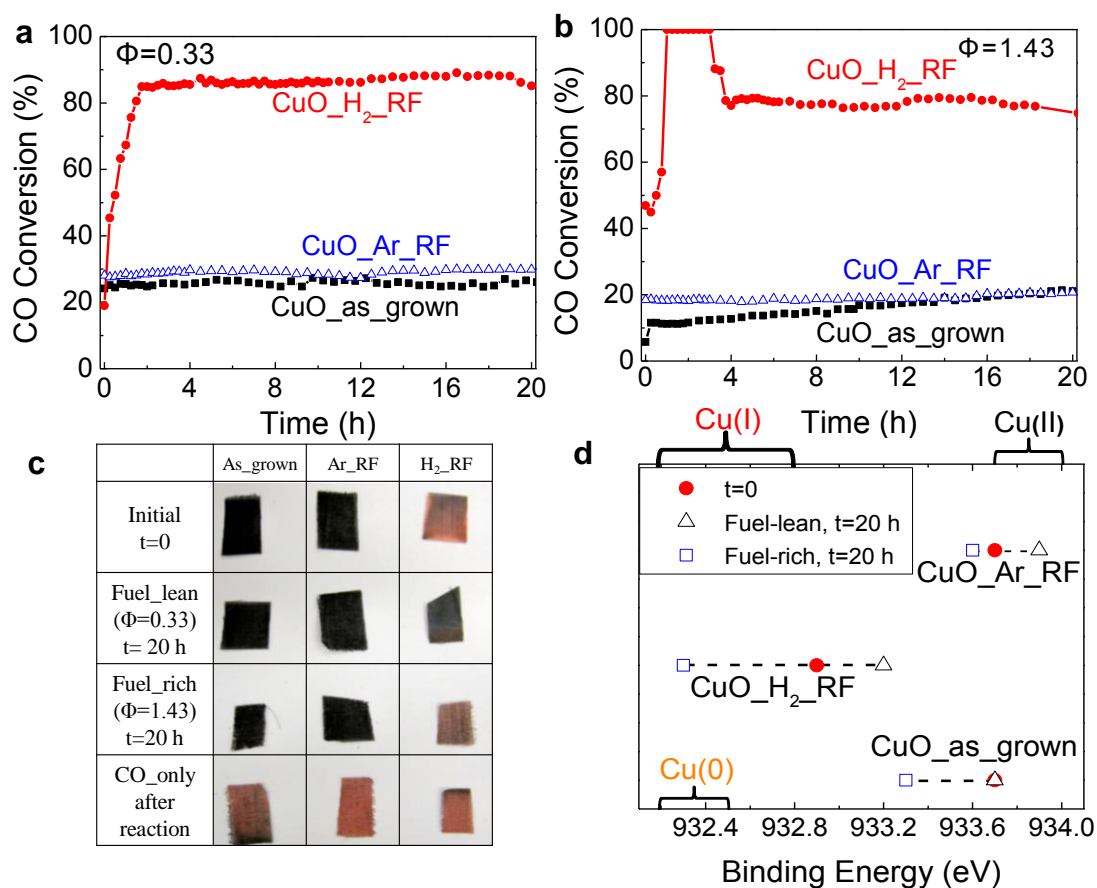
Figure 3.2 CO conversion percentage over the CuO_as_grown, CuO_Ar_RF and CuO_H₂_RF NWs in the (a) fuel-lean (inflow: 2.0 vol.% CO and 3.0 vol.% O₂ balanced in He, Φ=0.33) and (b) fuel-rich (inflow: 2.0 vol.% CO and 0.7 vol.% O₂ balanced in He, Φ=1.43) conditions at 140°C and 1 atm; (c) photographs and (d) binding energy of the CuO_as_grown, CuO_Ar_RF and CuO_H₂_RF NWs at the initial state t=0 and 20 h after testing in the fuel-lean and fuel-rich conditions respectively. The last row of (c) shows photographs of the three NWs after reaction with CO (inflow: 2.0 vol.% CO balanced in He, 140°C, 1 atm) .

38

The catalytic activity of these three types of CuO NWs can vary with time depending on the oxidation state of copper and the stoichiometry of the CO and O_2 mixture. In the fuel-lean case (Figure 3.2a), for example, the CO conversion percentage is stable for more than 20 h over the CuO_as_grown and CuO_Ar_RF NWs catalysts, but decreases slightly over the CuO_H$_2$_RF NWs. These changes can be attributed to the change of oxidation states of Cu. As shown in Figure 3.2c (the 3rd column), the color of CuO_H$_2$_RF NWs changes from red to black after testing in the fuel-lean condition for 20 h, suggesting that Cu has been oxidized. The XPS analysis (Figure 3.2d) shows that the oxidation state of Cu in the CuO_H$_2$_RF NWs has shifted from Cu(I) to Cu(II) to some extent after 20 h of testing, so the decrease in the catalytic activity of CuO_H$_2$_RF NWs (Figure 3.2a) supports that Cu(I) is more active than Cu(II). The XPS analysis (Figure 3.2d) indicates that the oxidation states of Cu in both the CuO_as_grown NWs and CuO_Ar_RF NWs remain as Cu(II) after 20 h of testing, so their catalytic activity remains stable (Figure 3.2a).

Similarly, the catalytic activity of these CuO NWs also varies with time in the fuel-rich condition. As shown in Figure 3.2b, after the initial stabilization period, the CO conversion percentage increases gradually over both CuO_as_grown and CuO_Ar_RF NWs, but decreases over CuO_H$_2$_RF NWs. The oxidation states of Cu in these NWs have changed as shown by the colors of the samples (Figure 3.2c, the 3rd row) and the XPS analysis (Figure 3.2d). Specifically, the oxidation states of Cu in both CuO_as_grown and CuO_Ar_RF NWs have been reduced by CO to Cu(I) to some extent, so their catalytic activity increases with time. Similarly, the oxidation

39

state of Cu in CuO_H$_2$_RF NWs is reduced towards Cu(0) on the basis of the XPS analysis (Figure 3.2d), and the corresponding reduced catalytic activity is probably due to the decrease of the lattice oxygen on the surface of Cu(0) [87]. All the time dependent catalytic activity for these NWs in both fuel-lean and fuel-rich conditions is consistent with the fact that Cu(I) is more active than Cu(II) in the catalytic CO oxidation process.

3.3.2. Analysis of chemical kinetics

We further studied the reaction kinetics of the three CuO NWs. In our tube reactor, gas phase species diffusion is much faster than convection so that convection is the controlling transport mechanism. The estimated time scales for convection and reaction at 140°C are 10^{-2} s and 10^3 s, respectively, so our experiments were conducted at the kinetics controlled region. The reaction kinetics of the three CuO NWs was analyzed in the fuel-lean condition after the initial stabilization of the catalysts. We assumed that the oxidation of CO occurs through a one-step global reaction:

$$CO + \frac{1}{2}O_2 \rightarrow CO_2 \tag{3.2}$$

, and the reaction rate of CO (r, mol/(L•s)) can be expressed in the form of

$$r = -\frac{d[CO]}{dt} = A\exp(-\frac{E_a}{RT})[O_2]^a[CO]^b \tag{3.3}$$

40

, where E_a is the apparent activation energy (kJ/mol), A is the pre-exponential factor, a and b are the reaction orders of O_2 and CO, respectively. We measured r over a range of inflow of CO percentages (1.5 − 3.0 vol.%), O_2 percentages (1.5 − 4.0 vol.%), and temperatures (105 − 140°C), and did a linear fitting by taking the natural log of both sides of Eq. (3.3) to obtain E_a, A, a and b, which are shown listed in Table 3.1. The calculated and experimental reaction rates as functions of O_2 and CO mole fractions are also compared in Figure 3.3a and 3.3b to illustrate the good quality of the fitting. These three CuO NWs share some similarities in their reaction orders. First, the reaction orders of O_2 are all close to zero, indicating that the re-oxidation of the reduced surface lattice of CuO by the gas phase O_2 is fast comparing to other intermediate reaction steps [85], leading to a weak dependence of the reaction rate on the gas phase O_2 concentration. Second, the reaction orders of CO are all close to 1, indicating that the CO conversion percentage highly depends on the gas phase CO concentration. Similarly to our previous analysis of CH_4 oxidation [85], the strong dependence of reaction rate on the CO concentration indicates that CO oxidation by the surface lattice oxygen is probably the rate determining step. Nevertheless, the three CuO NWs have quite different E_as, in the sequence of CuO_H$_2$_RF < CuO_Ar_RF < CuO_as_grown, which is consistent with the enhancement from grain boundaries and different oxidation states of Cu. Importantly, all the CuO NWs are more effective than the commercial CuO powder (100 − 200 μm) with a higher reported E_a of 124 kJ/mol [93].

Table 3.1 Fitted reaction orders, apparent activation energy and pre-exponential factors for CO oxidation over the CuO_as_grown, CuO_Ar_RF and CuO_H$_2$_RF NWs[a]

	a (O_2)	b (CO)	E_a (kJ/mol)	ln A
CuO_as_grown	-0.08	0.80	115	24.99
CuO_Ar_RF	0.05	0.87	97	20.90
CuO_H$_2$_RF	0.04	0.65	79	15.48

[a] Experimental conditions: The inflow percentages of CO and O_2 are in the range of 1.5 – 3.0 vol.% and 1.5 – 4.0 vol.%, respectively and the temperature varies from 105 to 140°C.
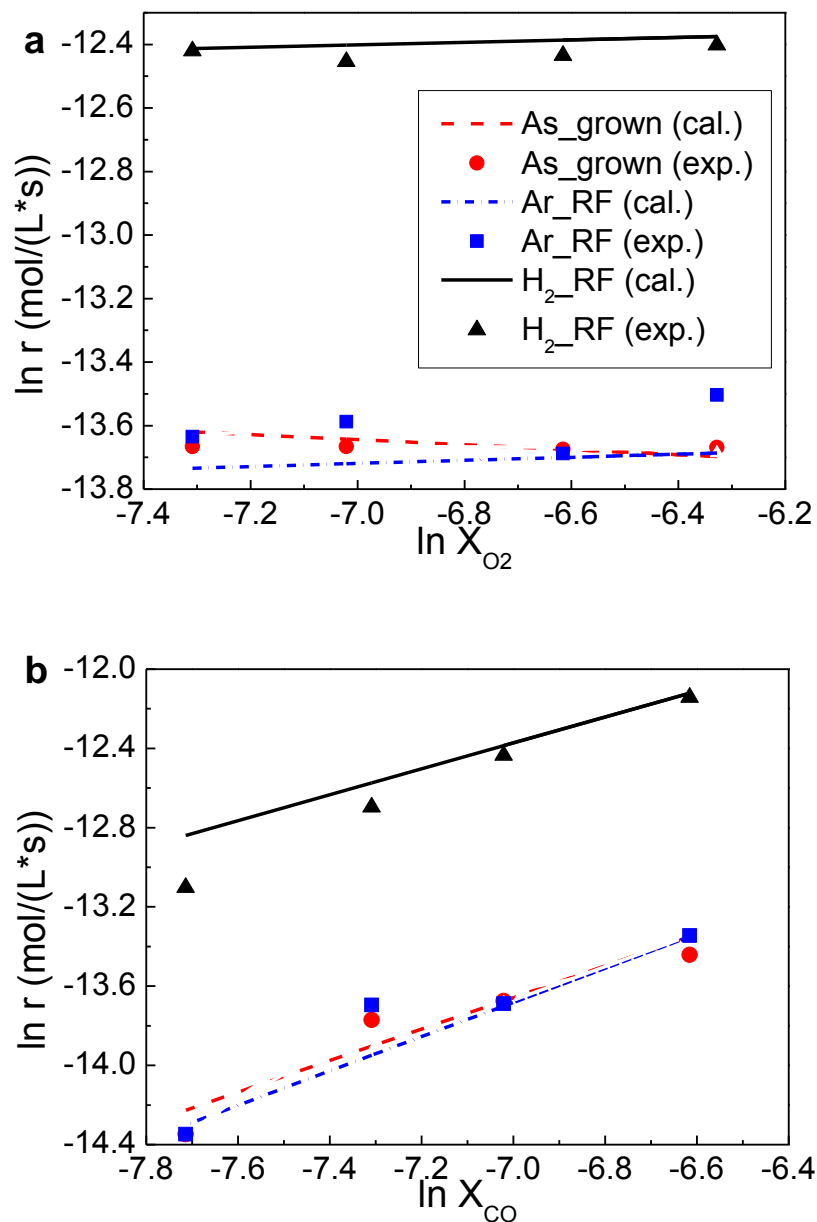
Figure 3.3 Calculated (lines) and experimental (symbols) reaction rates of CO over

the CuO_as_grown, CuO_Ar_RF and CuO_H$_2$_RF NWs at 140 ^{o}C as functions of the

mole fractions of (a) O$_2$ and (b) CO. The inflow percentages of CO and O$_2$ are in the

range of 1.5 – 3.0 vol.% and 1.5 – 4.0 vol.%, respectively and the temperature varies from 105 to 140°C.

3.3.3. Bulk oxygen diffusion

Although many previous studies have observed the similar high activity of Cu(I) comparing to Cu(II) in catalyzing the oxidation of CO, there is no consensus in the causes. Jernigan and Somorjai [88] investigated the CO oxidation over different copper oxides thin films and proposed that the relative low activity of CuO is caused by its lack of ability to dissociate gas phase oxygen as an insulator. The same conclusion was reached by White et al.[89] when studying the CO oxidation over supported Cu$_2$O NPs on silica gel and CuO NPs. Huang et al. [87] studied the CO oxidation over bulk copper oxides and suggested that Cu(I) can seize or release surface lattice oxygen more readily than Cu(II). Sadykov et al.[90] recently applied CO pulses to study the kinetics of CO oxidation over CuO and CuO$_x$, and found that the diffusion of oxygen atoms from the bulk to the surface of copper oxides also plays an important role in the catalytic process. We believe that the bulk oxygen diffusion to the surface is also significant for the catalytic properties of the three CuO NWs studied here. As evidenced by the fuel-lean case, after 20 h of testing, although the several top layers of all the three catalysts have been oxidized to Cu(II) (Figure 3.2d), the catalytic activity of the CuO_H$_2$_RF NWs is much higher than the other two (Figure 3.2a). It implies that bulk oxygen also participates in the catalytic oxidation reaction of CO and

bulk oxygen diffuses to the surface faster in CuO_H$_2$_RF NWs than in the other two

CuO NWs, leading to a high oxidation rate of CO.
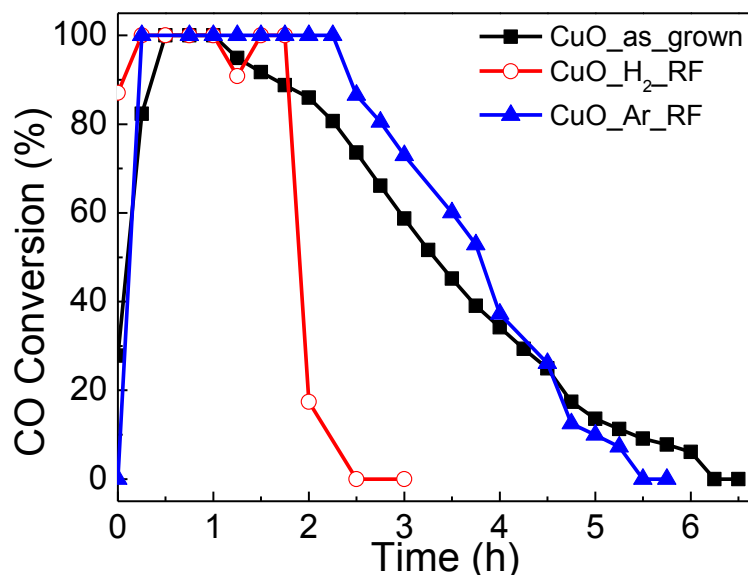
Figure 3.4 Conversion percentages of CO over the CuO_as_grown, CuO_Ar_RF

and CuO_H$_2$_RF NWs in the absence of O$_2$. Experimental conditions: 140 ^{o}C, 1 atm,

and the inflow gas is consisted of 2.0 vol.% CO balanced in He.

To compare the bulk oxygen diffusion rates in the three CuO NWs, we

experimentally investigated the oxidation reaction between CO and these NWs

without the presence of gas phase O$_2$, using the inflow gas of 2.0 vol.% CO balanced

in He at 140°C and 1 atm. After few hours of testing, all the three NWs are reduced by

CO as evidenced by their red color (Figure 3.2c, the bottom row). The conversion

percentages of CO over the three NWs are plotted as a function of time in Figure 3.4.

The total amount of oxygen in the three NWs can be calculated by integrating the amount of oxidized CO over the test period in Figure 3.4 and the ratio of CuO_as_grown:CuO_Ar_RF:CuO_H$_2$_RF is 1.00:1.09:0.57. The much lower oxygen content in CuO_H$_2$_RF is consistent with the fact that most Cu is in the lower oxidation state Cu(I). The average oxidation rate of CO, which is proportional to the bulk diffusion rate of oxygen in the NWs, is calculated by dividing the total amount of oxygen over the total reaction time, and the ratio of CuO_as_grown:CuO_Ar_RF:CuO_H$_2$_RF is 1.00:1.24:1.46. First of all, the two RF plasma-treated CuO NWs have higher bulk diffusion rates of oxygen because of the grain boundaries generated by the plasma impact. More importantly, the bulk oxygen diffusion rate in CuO_H$_2$_RF NWs is higher than that of oxygen in CuO_Ar_RF NWs, indicating that bulk oxygen diffusion is indeed faster in Cu$_2$O than that in CuO, as suggested by the above fuel-lean case test. Therefore, the faster bulk oxygen diffusion rate in Cu$_2$O is likely to be a main reason for the higher catalytic activity of Cu(I) than Cu(II) in these NWs.

3.4. Conclusion

In summary, we have enhanced the catalytic activity of CuO by a brief Ar or H$_2$ RF plasma treatment. The CO oxidation percentage is increased from 24% over CuO_as_grown NWs to 29% and 85% over CuO_Ar_RF and CuO_H$_2$_RF NWs respectively at 140°C in the fuel lean condition, and similar level of improvement was observed for the fuel rich condition as well. The enhancement from the plasma

treatment is caused by the creation of grain boundaries and the reduction of Cu(II) to the more active Cu(I). Moreover, the fact that Cu(I) is more active than Cu(II) is also supported by the exacted activation energies of CO oxidation over the CuO_as_grown (115 kJ/mol), CuO_Ar_RF (97 kJ/mol) and CuO_H$_2$_RF NWs (79 kJ/mol) though kinetic analysis. The reason for the higher activity of Cu(I) is that the bulk oxygen in the three CuO NWs also participates in the catalytic oxidation of CO and the diffusion rate of bulk oxygen to surface is higher in CuO_H$_2$_RF NWs.

Chapter 4. Decorate CuO NWs with Co_3O_4 NPs for Higher Catalytic Activity with Sol-flame Method

4.1. Introduction

In Chapter 3, the catalytic activity of CuO NWs was increased by plasma treatment, due to the creation of grain boundaries, and the reduction from Cu (II) to more reactive Cu (I). However, this was only based on the Cu system. Here, this work is extended to more active materials, Co_3O_4. By introducing Co in CuO NWs system, the catalytic activity is expected to enhance dramatically. The most straightforward way to combine these two is to decorate the CuO NW backbones with Co_3O_4 NPs (Co_3O_4@CuO). The exposed Co_3O_4 NPs on the surface can give rise to the catalytic activity [94]. To achieve the best performance, it is highly desirable to synthesize this hybrid Co_3O_4@CuO structures with several simultaneous qualities: high coverage density of NPs with minimal aggregation, good morphology control, minimal contamination from processing, and high yield, in a scalable and controllable manner. So far, however, the reported methods to fabricate the NP@NW structures, such as impregnation and deposition−precipitation,[95, 96] electrochemical deposition,[97] physical/chemical vapor deposition,[98] self-assembly[99, 100] and thermal growth,[94, 101] either require tedious preparation processes and/or expensive equipments, or lack control over the size and morphology of the NW and NP building blocks, and cannot, therefore, meet the above requirements.

Flame synthesis, in comparison to many other existing synthesis methods (e.g., the hydrothermal method and chemical vapor deposition), provides unique and important advantages of rapid material growth rate, low cost, versatility and scalability. Flame synthesis has been successfully used to grow various 1-D simple binary metal oxide nanostructures, such as ZnO nanorods [102, 103], Fe_3O_4 nanorods, [104], α-Fe_2O_3 nanoflakes and CuO NWs [78], $W_{18}O_{49}$ NWs, WO_3 NWs and nanotubes [105], α-MoO_3 nanobelts [106] and γ-Fe_2O_3 NWs [107]. Flame synthesis has also been successfully used to grow various hybrid NPs [108], such as Al_2O_3-TiO_2 mixed oxides [109], TiO_2 coated SiO_2, SiO_2 coated TiO_2 [110], and $YB_2Cu_3O_x$ superconducting oxide [111]. However, flame synthesis of decorated NWs has not been reported in the literature.

Here, we report a general *sol-flame* method to decorate arrays of CuO NWs with Co_3O_4 NPs in a simple, scalable, and controllable manner. In particular, our sol-flame method decorates NWs with chains of NPs in a hierarchical morphology. The sol-flame method combines the merits of the sol-gel method,[112] dip-coating, and flame spray pyrolysis[113-115]. High quality of Co_3O_4@CuO hybrid NWs were synthesized, and used to catalyze the methane oxidation reaction. The control of the morphology was studied. In addition, the sol-flame method was compared to the conventional thermal annealing method to show the advantages.

4.2. Experimental specifications

4.2.1. Synthesis of Co_3O_4 NPs @ CuO NWs

The sol-flame is schematically illustrated together with corresponding SEM images in Figure 4.1. First, the CuO NWs are grown on a substrate (Figure 4.1a) by thermal annealing method described in Chapter 2, and the Co_3O_4 NP precursor made of metal salt solution is prepared by the sol-gel method (details in Chapter 5). Next, the NP precursor solution is coated uniformly over the entire surface of CuO NWs by dip-coating. After drying in air (or N_2), a Co salt shell is formed on the surface of the NWs (Figure 4.1b and 4.2). Finally, the metal salt-coated NWs are annealed over a flame for a few seconds, and consequently the NWs are decorated with a high coverage density of NP chains fanning radially outward from the NW axes (Figure 4.1c). During the high temperature flame treatment, the remaining solvent in the Co salt shell readily evaporates and combusts, producing gases such as H_2O and CO_2[116] that flow radially outwards, blowing the Co salt precursors away from the NWs. These Co salt precursors decompose chemically to the final Co_3O_4 and nucleate locally, forming the NP chain morphology. Moreover, the high temperature of the flame and short annealing time lead to high nucleation rate and suppress grain growth, and hence ensure small and less aggregated NPs around the NWs (Figure 4.1c). The short annealing time is facilitated by the fast heating rate of the substrate by the flame. Additionally, the sol-flame method, compared to the traditional flame spray pyrolysis method [113-115], localizes the coating and nucleation process in the proximity of the

target NWs, enabling conformal coating with fine control, and it simplifies the particle deposition process and equipment requirement.
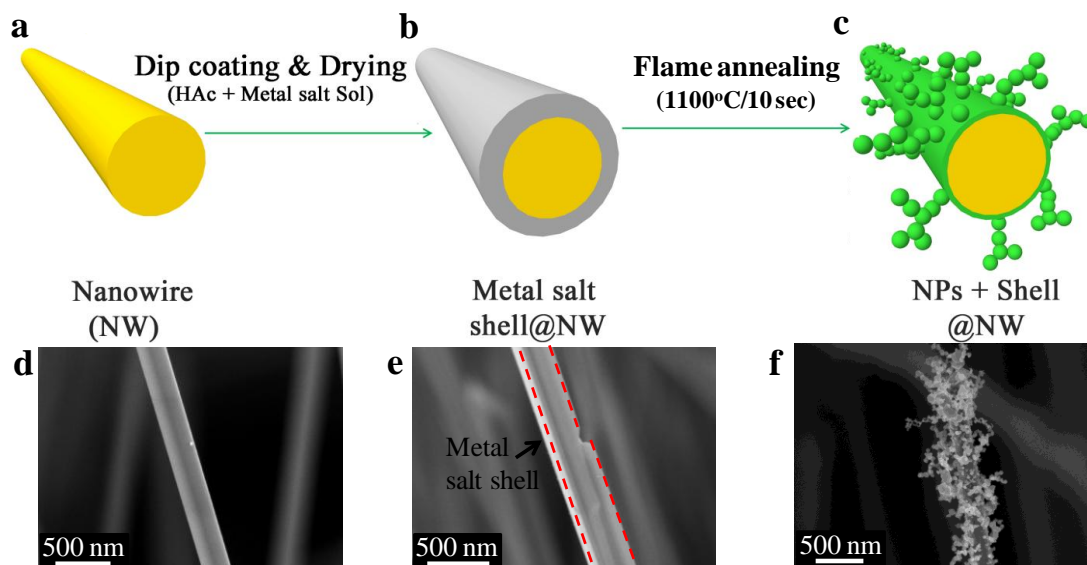
Figure 4.1 Schematic illustration of the general sol-flame synthesis process for hybrid NP@NW nanostructures. The NWs (a) are dip-coated with the precursor solution of NPs and then dried in air (or N_2) to form a metal salt shell on the NWs. Then coated NWs (b) are annealed in the flame, forming a NP-chain morphology (c). The corresponding SEM images of (d) CuO NW, (e) $Co(CH_3COO)_2$ shell@CuO NW and (f) Co_3O_4 NP@CuO NW.
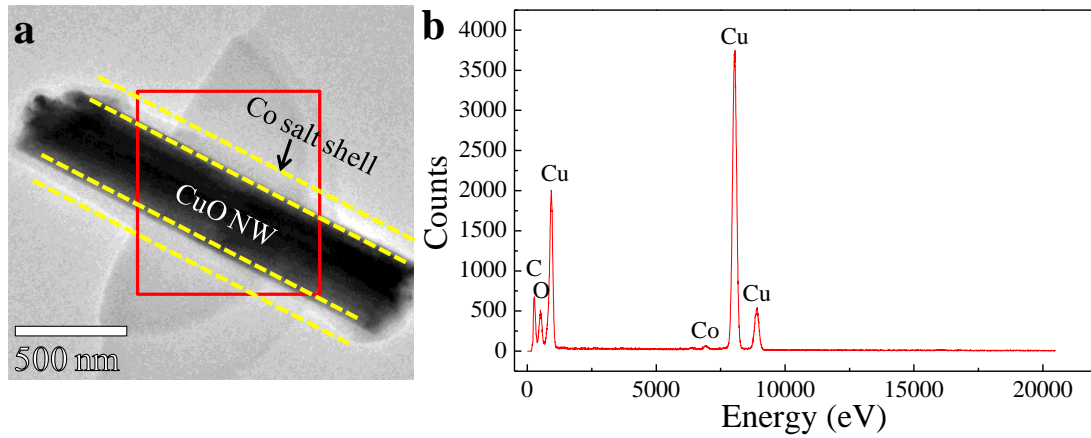
Figure 4.2 (a) TEM image and (b) TEM-EDS spectrum of the cobalt salt shell@CuO NW. The TEM-EDS spectrum shows the elements present in the boxed region in (a).

4.2.2. *Measurement of the catalytic activity of hybrid metal oxide NWs*

One of the major advantages of the hybrid NP@NW structure is the increased loading of active materials, which is beneficial when the NPs are involved in surface reactions. To illustrate this enhanced loading effect, we measured the catalytic activities of the hybrid Co_3O_4 NPs@CuO NWs for methane (CH_4) oxidation reaction in a custom-built tube flow reactor [85, 117] described in Chpater 2. The inflow was a mixture of 1.5 vol.% CH_4 and 6.0 vol.% O_2 diluted in helium, with a total flow rate of 100 sccm. The CH_4 conversion percentage was defined as

$$CH_4\% = \frac{X_{CH_4}(\text{initial}) - X_{CH_4}(\text{effluent})}{X_{CH_4}(\text{initial})} \tag{4.1}$$

, where X_{CH_4} (initial) and X_{CH_4} (effluent) were the CH_4 mole fractions in the inflowing and effluent streams, respectively.

52

4.3.   Results and discussion

4.3.1.   Characterizations of $Co_3O_4@CuO$

The scanning electron microscope (SEM, FEI XL30 Sirion, 5kV) images in Figure 4.1d-f show the CuO NWs at different stages of the synthesis. The CuO NWs were grown by annealing Cu foil at 520^oC in air for two days through the solid diffusion mechanism (Figure 4.1d).[79, 85, 117] The as-grown CuO NWs were first coated with a thin layer of cobalt salt shell after the dip-coating step (Figure 4.1e and Figure 4.2) and the thin layer was transformed to Co_3O_4 NP chains after the flame annealing (Figure 4.1f). The $Co_3O_4@CuO$ was further examined using a transmission electron microscope (TEM, Philips CM20 FEG, 200 kV, Figure 4.3a). The diameter of the Co_3O_4 NPs is about 100 nm, and the particles uniformly cover the surface of the CuO NW. These Co_3O_4 NPs clearly nucleate as individual NPs without agglomeration into large particles, which is a highly desired feature for catalysts [69, 118]. The interface between NWs and NPs marked in the boxed region of Figure 4.3a was further characterized by a high resolution TEM (HRTEM) as shown in Figure 4.3b. The CuO NW is single crystal with a [-1 1 1] growth direction and the attached Co_3O_4 NP is also highly crystalline. Interestingly, there is a thin Co_3O_4 layer of approximately 4 nm thickness between the CuO NWs and Co_3O_4 NPs, which would ensure good electrical contact and charge transport between the NPs and NWs in applications such as lithium ion batteries [97]. The phase homogeneity and crystallinity of the NP chains are further confirmed by the selected area electron diffraction (SAED) pattern (Figure 4.3c).
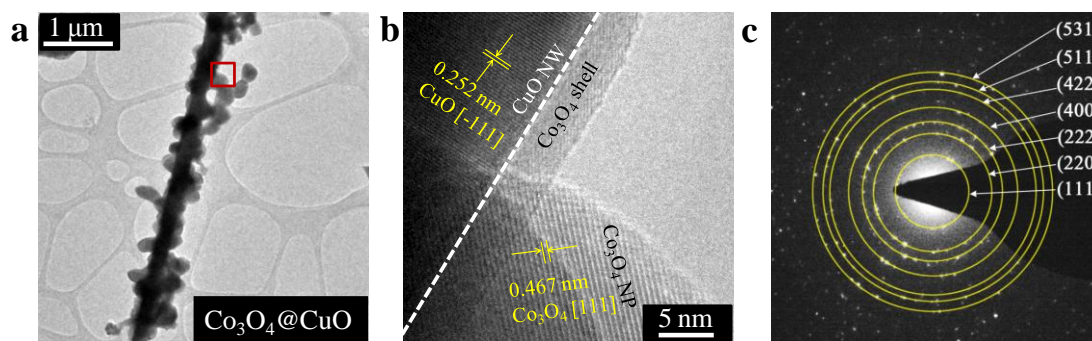
Figure 4.3 (a) TEM (b) HRTEM images and (c) selected area electron diffraction (SAED) pattern of Co_3O_4@CuO. All the ring patterns are indexed to cubic spinel Co_3O_4. The HRTEM shows the boxed region in (a).

4.3.2. Morphology control

Our limited study shows that the sol-flame method offers control, though not precisely, over the size and coverage density of the NPs through control of the metal salt precursor concentration, the number of dip coats, the flame annealing temperature and the annealing duration. The NP size can be varied from tens to hundreds of nm, and the number of NPs per micron of NW can range from tens to hundreds. For example, increasing the number of dip coats increases the metal salt loading on the NW surface, leading to larger and more densely arranged NPs. Figure 4.4 illustrates Co_3O_4@CuO structures for which the CuO NWs were dipped into the 0.1 M Co salt solution 1 time (Figure 4.4a), 3 times (Figure 4.4b) and 5 times (Figure 4.4c), respectively. The average size of the Co_3O_4 NPs increases with the number of dip coats, with diameters of 50 nm, 100 nm and 180 nm for 1 time, 3 times and 5 times dip-coating, respectively. Simultaneously, the coverage density of the Co_3O_4 NPs also

54

increases from sparse to dense coverage with the increasing number of coats. Besides

the number of dip coats, the solution concentration has similar effects. Increasing the

metal salt concentration in the initial sol solution results in larger NP size and higher

coverage density, because more metal salt is coated on the surface of NWs (similar

effect to the number of dip-coats). Additionally, the NP coverage density can be

independently changed with respect to the NP size by applying dip-coating and flame

annealing process for multi-times.
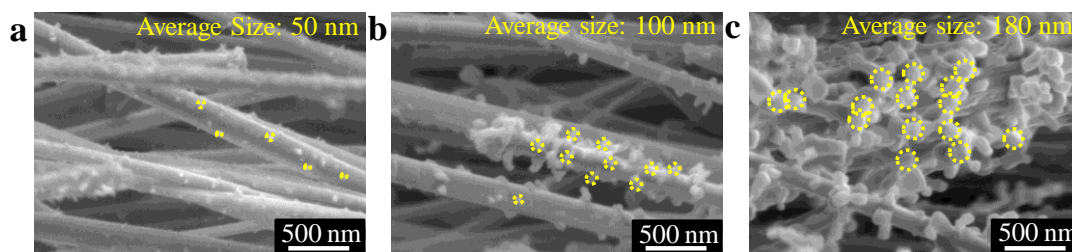
Figure 4.4 The size and coverage density of NPs can be controlled by varying the number of dip-coating. SEM images of Co_3O_4@CuO synthesized by dip-coating CuO NWs in 0.10 M $Co(CH_3COO)_2$ for (A) 1 time, with an average NP size of 50 nm, (B) 3 times, with an average NP size of 100 nm and (C) 5 times, with an average NP size of 180 nm. For all the samples, the flame annealing temperature was 1100^oC and annealing duration was 1 min.

4.3.3. Comparison of flame annealing to furnace annealing

The novel and unique aspect of the sol-flame method is the flame annealing step, in comparison to the furnace annealing. To explore the benefits of flame annealing, we conducted control experiments to anneal Co salt-coated CuO NWs under three different annealing conditions: 1) furnace annealing in air at 600^oC for 3 h (with a

55

heating rate of $5^{\circ}C$/min), 2) flame annealing at $600^{\circ}C$ for 1 min, and 3) flame annealing at $1100^{\circ}C$ for 1 min. For the furnace annealing case, large Co_3O_4 NPs with an average diameter of 200nm are sparsely dispersed on the surface of the CuO NWs (Figure 4.5a). However, for the flame annealing at the same temperature, smaller Co_3O_4 NPs with an average diameter of 100nm densely cover the surface of the CuO NWs (Figure 4.5b). Furthermore, for the flame annealing at much higher temperature ($1100^{\circ}C$), the NPs not only have smaller average size and higher coverage density, but also from the unique NP chain structure with much higher loading of Co_3O_4 NPs per CuO NW. Two properties of the flame contribute to the NP morphology differences observed in Figure 4.5. First, the flame annealing process has much higher heating rate than the furnace annealing process even at the same annealing temperature, which imposes a sudden temperature rise on the metal salt coated NWs. The remaining solvent in the metal salt shell immediately evaporates and combusts, producing gases such as H_2O and CO_2 that blow the metal salt precursors away from the NWs, and simultaneously the metal salt precursors decompose to metal or metal oxides, leading to the formation of the unique NP chain morphology. Second, the high heating rate of the flame also enables shorter time for annealing, which limits the time for the NP grain growth. Hence, smaller and less aggregated NPs are formed around the NWs for the flame annealing. In other words, one key difference between flame annealing and furnace annealing is the heating rate. Although high heating rate can be achieved by other means, such as hot air stream, flame is probably the simplest and cheapest method to achieve such fast heating rate.

(a) Furnace annealing: 600°C, 3 h   (b) Flame annealing: 600°C, 1 min   (c) Flame annealing: 1100°C, 1 min

1 μm   200 nm   1 μm
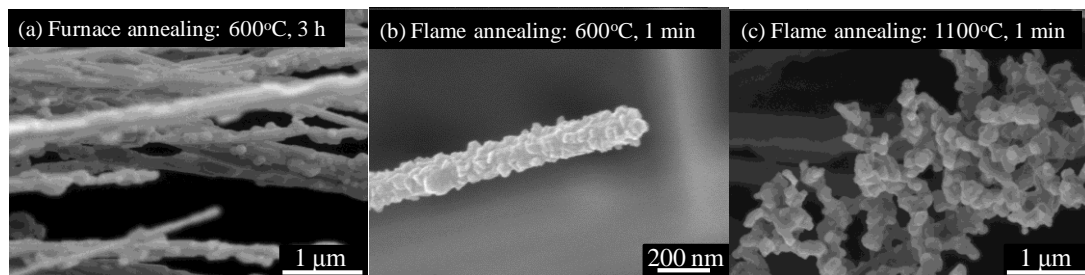
Figure 4.5 Comparison of conventional furnace annealing and flame annealing effects. SEM images of Co_3O_4@CuO synthesized by annealing Co salt-coated CuO NWs in (a) furnace at 600°C for 3 h (with a heating rate of 5°C/min), (b) flame at 600°C for 1 min, and (c) flame at 1100°C for 1 min.

4.3.4. Catalytic activity of Co_3O_4@CuO

The merits of flame annealing become even more obvious when comparing the catalytic activities of the above three Co_3O_4 NPs@CuO NWs for methane oxidation since Co_3O_4 is a well-known catalyst for this process [56, 119]. As shown in Figure 4.6, first, the catalytic activity of all the Co_3O_4 NPs decorated CuO NWs is higher than that of the bare CuO NWs, which exhibit the advantages of the hybrid NWs. More importantly, the methane conversion percentages for the two flame-annealed samples, especially the 1100°C sample, are much higher than those for the furnace-annealed sample over the entire tested temperature range. These results are consistent with the loading of catalytic Co_3O_4 NPs (Figure 4.5), where the NP-chain morphology has the highest surface area of Co_3O_4 per CuO NW. This comparison illustrates the benefit of using flame annealing to achieve high surface area structures, which is important for

57

not only catalysis, but also other applications, such as gas sensing and photoelectrochemical (PEC) water splitting.
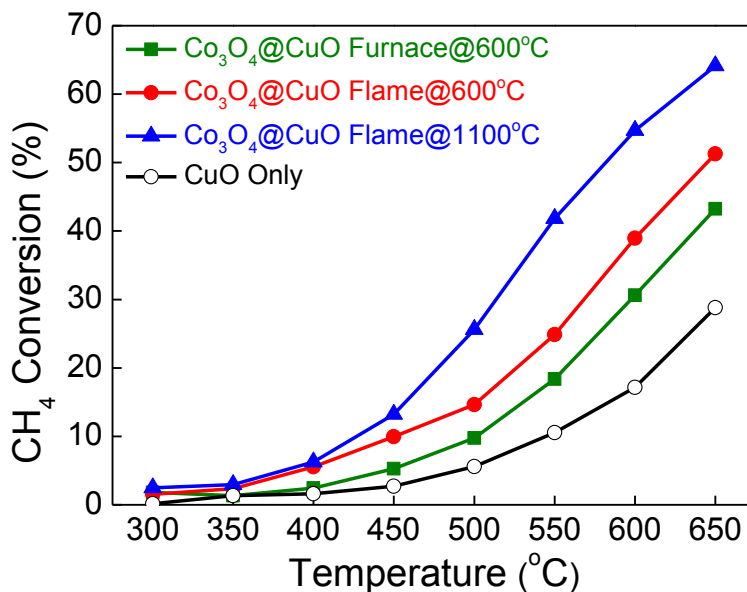
Figure 4.6 Methane conversion percentages at different temperatures over CuO NWs and Co_3O_4@CuO catalysts, which were synthesized by annealing Co salt-coated CuO NWs in different conditions, as shown in Figure 4.5.

4.4. Conclusion

We have decorated CuO NWs with more active Co_3O_4 NPs to further increase the catalytic activity of the NW catalysts. High density Co_3O_4 NP chain attached CuO NWs were fabricated with the newly developed sol-flame method. The introduction of Co_3O_4 NPs greatly increased the catalytic activity of CuO. Moreover, the sol-flame method provides larger loading and higher surface area, showing advantages over the conventional fabrication methods. Notably, both the size and the coverage density of

the NPs can be controlled to a certain degree by varying the concentration of the initial precursor solution and the number of dip-coated layers, and further research is needed for achieving more precise morphology control of NPs. The unique aspects of the sol-flame method are the ultrafast heating rate and high temperature of the flame, which enable rapid solvent evaporation and combustion, and nucleation of NPs in the vicinity of the NWs without significant NP agglomeration, leading to the unique NP chain morphology on NWs.

Chapter 5. Sol-flame Method to Synthesize Hybrid NWs

5.1.   Introduction

In Chapter 4, the newly developed sol-flame method was used to synthesize the Co_3O_4 NPs@CuO NWs heterogeneous nanostructures. Considering the generality of sol-gel method for the NP precursors, and the simple fabrication process, this method is extended to fabricate other hybrid NWs.

The hybrid or heterogeneous NWs composed of different materials and morphologies, such as axially modulated NWs, core/shell NWs, NP decorated NWs, and doped NWs, provide even more exciting opportunities to tailor their physical and chemical properties by independently controlling the chemical compositions and physical morphologies of the individual components. Hybrid NWs have already demonstrated great potential in diverse application areas, including lithium ion batteries [97, 120, 121], gas sensors [98, 99], photoelectrochemical (PEC) water splitting devices [94, 99, 122, 123] and heterogeneous catalysis [124]. For example, Cu NWs decorated with Fe_3O_4 NPs were used as a Li-ion battery anode and showed six times higher energy density than Fe_3O_4 NPs on planar Cu because of the larger loading of Fe_3O_4 NPs on the Cu NWs than on the planar Cu [97]. Fe-doped TiO_2 nanorods had more than twice higher photocatalytic activity than that of TiO_2 powders, firstly because the 1-D nanostructure enhances charge carriers transfer, and secondly because the doped Fe decreases the band gap of TiO_2 and hence increases light absorption [125].

In this chapter, the sol-flame method was used as a general strategy for the preparation of 1-D hybrid metal oxide nanomaterials by attaching NPs to or incorporating dopants into already grown NWs. With the same process described in 4.2, we have successfully synthesized a range of NP-chain decorated NWs (NP-chain@NW), NP-shell coated NWs (NP-shell@NW) and doped NWs, such as TiO_2@CuO, ZnO@WO_3, ZnO@CuO, Au@CuO and W-doped TiO_2 NWs. The key controlling factors for the sol-flame method were also discussed.

5.2.   Experimental Specifications

5.2.1. *Synthesis of hybrid metal oxide NWs*

The steps of the *sol-flame* method for the synthesis of hybrid metal oxide NWs are illustrated schematically in Figure 5.1, together with their corresponding scanning electron microscope (SEM, FEI XL30 Sirion, 5 kV) images. As described in Section 4.2, The sol-flame method includes three steps, namely 1) synthesis of metal oxide NW arrays and sol-gel preparation of NP precursors, 2) dip-coating and 3) rapid flame annealing. First, bare metal oxide NW arrays were grown on a substrate (Figure 5.1a) and the NP/dopants precursors were prepared separately by mixing their corresponding metal salts with acetic acid and then aged for 12 h before being used for dip coating. Next, the NW arrays were dipped into the precursor solution and withdrawn vertically at a constant speed of about 1.0 mm/sec in the ambient environment. The dip-coated NW arrays were subsequently dried in air, which evaporated most of the solvent and left a metal salt shell on the surface of the NWs

61

(Figure 5.1b). Finally, the metal salt-coated NWs were briefly annealed in the post-flame region of a premixed flame, which dissociated and oxidized the metal salt precursors, and evaporated and burned the remaining solvents.

Depending on the flame annealing condition and the material choices of NPs and NWs, three different types of hybrid metal oxide nanostructures were formed: 1) NW arrays coated with a shell of NPs (NP-shell@NW, Figure 5.1c, ZnO NP-shell@CuO NWs), when the metal salt-coated NWs were annealed at low temperature, 2) NW arrays radially coated with NP chains (NP-chain@NW, Figure 5.1d, ZnO NP-chains@CuO NWs), when the metal salt-coated NWs were annealed at relatively high temperature, and 3) doped NW arrays with unmodified NW morphology (Figure 5.1e, W-doped TiO_2 NWs), when the coated metal ions can diffuse into the lattice of NWs and the annealing temperature was high. In Section 5.3, we will discuss the effects of the flame annealing temperature, the annealing duration and the equivalence ratio on the morphologies of the final hybrid metal oxide NWs in detail.

a).   Synthesis of binary metal oxide nanowires (NWs)

CuO NW arrays: The CuO NWs were grown by the thermal annealing method which was described in detail in chapter 2 [79, 85, 117]. Perpendicularly aligned CuO NWs with a diameter range of 100 - 200 nm and an average length of 50 μm were formed through a solid diffusion mechanism.

TiO_2 NW arrays: The TiO_2 NW arrays was synthesized on TiO_2-seeded FTO substrates using hydrothermal method, and the details were reported in our previous work [126]. Prior to the NW growth, a TiO_2 polymeric sol prepared by the sol–gel

process was first spin-coated on the FTO and then annealed at 450 ℃ for 1 h as the seed layer (denoted as seeded-FTO). In a typical growth process, titanium (IV) butoxide (Aldrich Chemicals, 97%) was added into 50 ml of an aqueous HCl solution (25 ml of deionized (DI) water and 25 ml of concentrated HCl (38%)) under magnetic stirring. After stirring for another 5 min, the solution was poured into a Teflon-lined stainless steel autoclave (100 ml capacity) and pieces of the seeded-FTO substrates, which have been cleaned for 10 min using an ultrasonicator in a mixed solution of DI water, acetone, and isopropanol, were immersed in the solution. The autoclave was sealed and heated to the desired temperature (160 − 180 ℃) in an oven, held at the temperature for 6 h without stirring, removed from the oven, and allowed to cool down to room temperature naturally on a bench top. The obtained materials were washed with DI water followed by absolute ethanol and finally annealed at 450 ℃ for 1 h in air.

b).   *Preparation of metal salt solution and the dip-coating process*

The Zn, and Co metal salt precursor solutions with a typical total metal salt concentration of 0.02 - 0.1 M, were prepared by mixing their corresponding metal salts $(Zn(CH_3COO)_2\text{-}2H_2O$, 99%; $Co(CH_3COO)_2\text{-}4H_2O$, 99%; Sigma-Aldrich Chemicals) with Acetic acid $(CH_3COOH$, 99.7%, EMD Chemicals) and then aged for 12 h before being used for dip coating. For the preparation of W precursor doping solution (0.1M), tungstic acid $(H_2WO_4$, 0.25g) was dissolved into H_2O_2 (30 %, 6 ml) and then heated to 120-140°C until the solution volume was reduced to 1 ml. After cooling, 9 ml of 2-methoxyethanol (99%, Aldrich Chemicals) was added and well

63

mixed by stirring (10 min) and sonication (10 min). Prior to the dip coating, the metal oxide (CuO and TiO$_2$) NWs were first washed by IPA (Isopropyl alcohol) or EtOH (ethanol) to improve the coating/wetting quality of the NP precursor solution. The cleaned 1-D nanostructures were then dipped into the metal salt solution and withdrawn vertically at a constant speed (1.0 mm/sec), under the ambient condition. After withdrawal, the coated 1-D nanostructures were dried in air flow.

c).   Flame annealing

The premixed flame used for the sol-flame process was stabilized over a co-flow flat premixed flame burner (McKenna Burner) operating with CH$_4$ and H$_2$ as fuels, and air as the oxidizer. The annealing temperature in the post-flame region was controlled by adding plain steel cooling meshes (0.318cm wire spacing, 0.064cm wire diameter, McMaster-Carr) between the flame and the NW substrates, and was measured by a K-type thermocouple (1/16 inch bead size, Omega Engineering, Inc.). The typical flame annealing condition was at 1100°C (gas temperature at the substrate) for 1 min with an equivalence ratio (Φ) of 0.84 (the flow rates of CH$_4$, H$_2$, and air were 2.05, 4.64, and 36.7SLPM, respectively), unless otherwise specified.
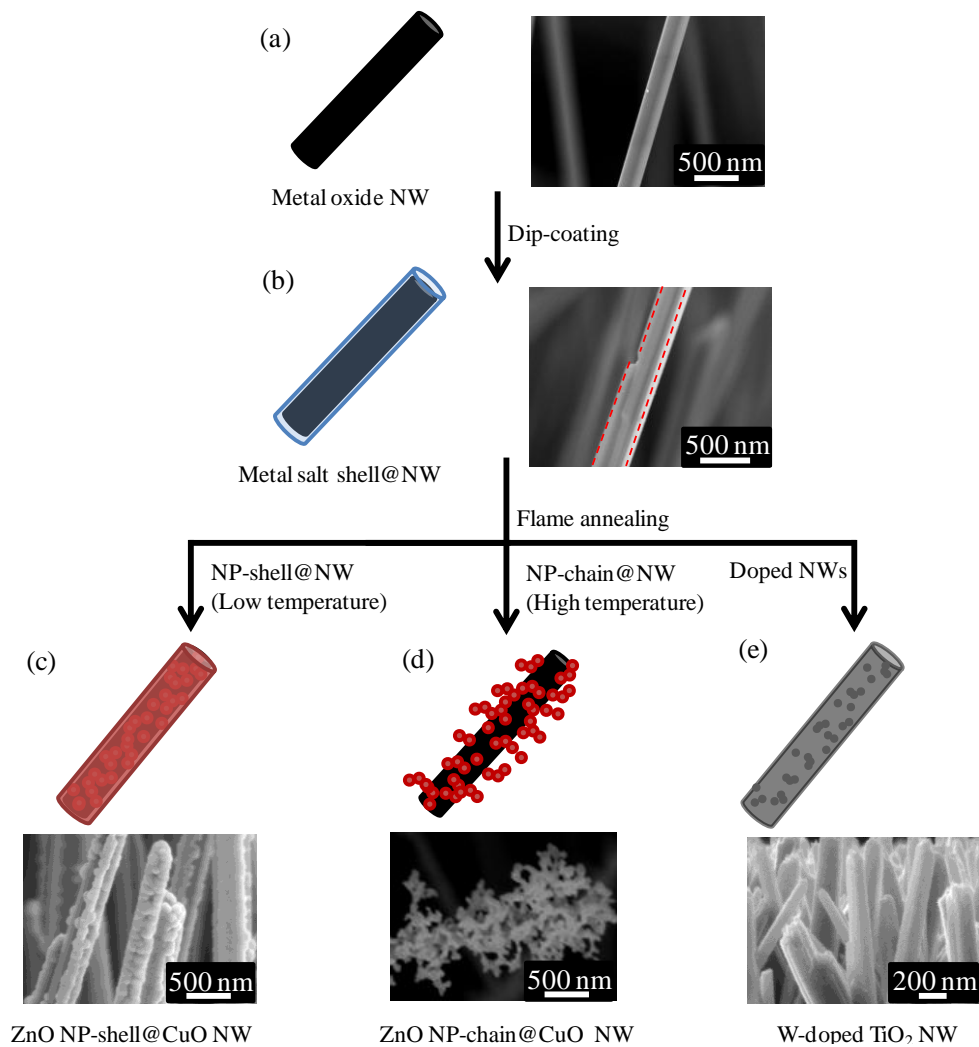
Figure 5.1 Schematic steps of the sol-flame method to synthesize different hybrid metal oxide NWs with corresponding SEM images.

5.3. Results and Discussion

5.3.1. NP-chain@NW heterogeneous structures

Beyond the example of Co_3O_4 NPs @ CuO NWs demonstrated in Chapter 4, the sol-flame method is a general method to decorate various metal oxide NWs with diverse binary metal oxide NPs through the independent selection of the NWs and the

NP precursors. TiO_2 (Figure 5.2), ZnO (Figure 5.3) and NiO NP (Figure 5.4) chains were respectively deposited onto CuO NW arrays on a copper mesh with the sol-flame method, and the HRTEM images in Figure 5.2-5.4 show that all these binary oxide NPs are single crystalline. It should be noted that when the NP and the NW tend to form stable complex, the formed NPs can be ternary oxide NPs formed by additional reactions between the NPs and NWs during the flame annealing step. For example, single crystal $ZnWO_4$ NPs [127] were formed on WO_3 NW arrays ($ZnWO_4@WO_3$) when zinc salt coated WO_3 NWs [105] were annealed in flame for 1 min (Figure 5.5). Similarly, $CoWO_4@WO_3$[128] (Figure 5.6) and $Fe_2O_3/Cu_xFe_{3-x}O_4@CuO$[129] (Figure 5.7) were synthesized by annealing Co salt coated WO_3 and Fe salt coated CuO NW arrays in flame, respectively. All these cases share common characteristics of 1) uniform and dense coverage of NP chains on NWs with a thin shell of the NP material covering the NWs first, 2) uniform particle decoration over the entire NW growth substrate, and 3) highly crystalline and minimally aggregated NPs.
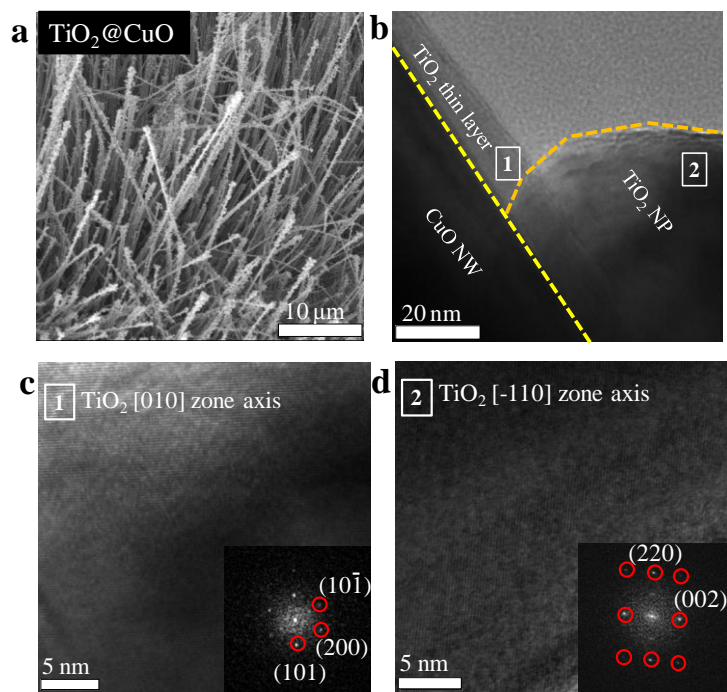
Figure 5.2 (a) SEM, (b) TEM image of TiO$_2$@CuO at the interfacial region, and (c, d) HRTEM images of the boxed region 1 and 2 in (b), respectively. The insets of (c) and (d) show corresponding FFT (Fast Fourier Transforms) patterns, indicating that both NP and shell are rutile phase of TiO$_2$ with high crystallinity.
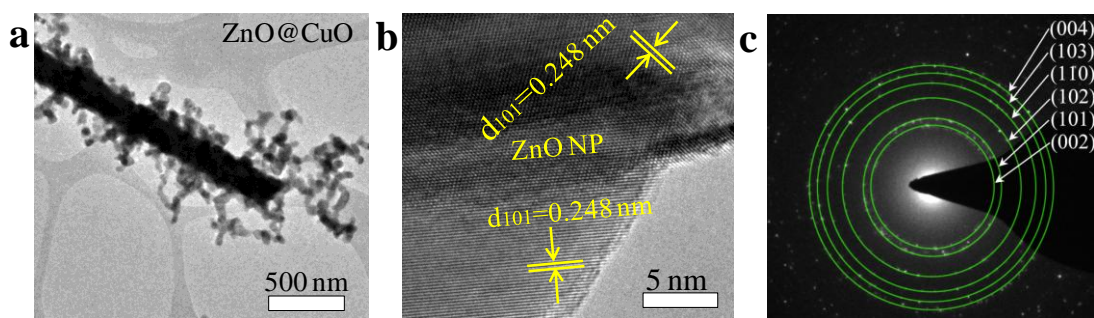
Figure 5.3 (a) TEM image of ZnO@CuO, (b) HRTEM image and (c) SAED pattern of NPs. All the ring patterns are indexed to hexagonal (wurtzite) phase of ZnO.
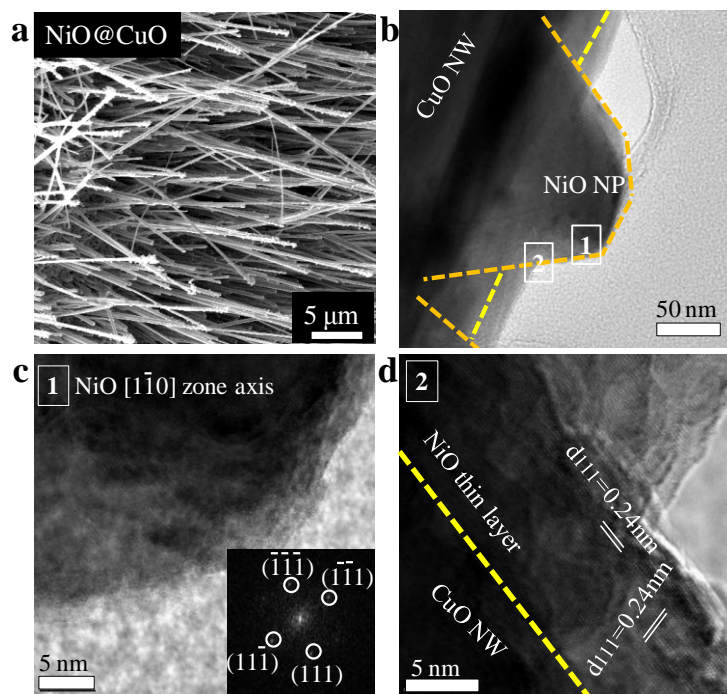
Figure 5.4 (a) SEM image of NiO@CuO, (b) TEM image of interfacial region and (c, d) HRTEM images of the boxed region 1 and 2 in (b), respectively. The inset of (c) shows its FFT pattern. The HRTEM images and FFT pattern indicate that both NPs and shell are cubic (rocksalt) NiO with high crystallinity.
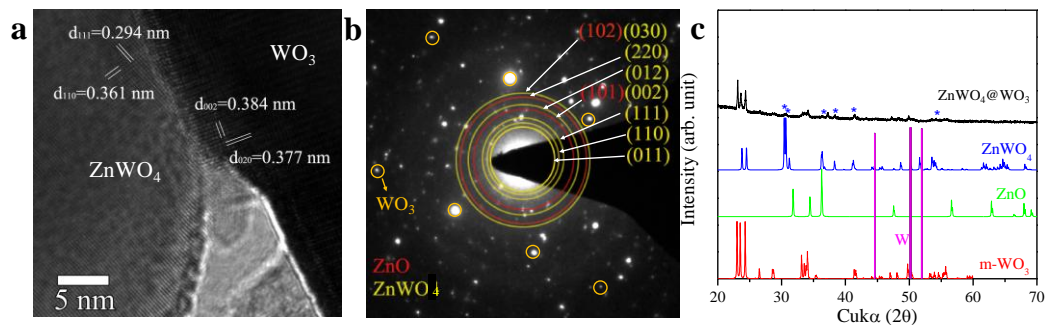
Figure 5.5 (a) HRTEM image, (b) SAED pattern and (c) XRD pattern of $ZnWO_4@WO_3$. All the SAED ring patterns are indexed to $ZnWO_4$, with some of them also close to ZnO. Since the HRTEM and XRD pattern matches $ZnWO_4$ well, it is

highly possible that the NPs are composed of the single crystal monoclinic (wolframite) $ZnWO_4$.
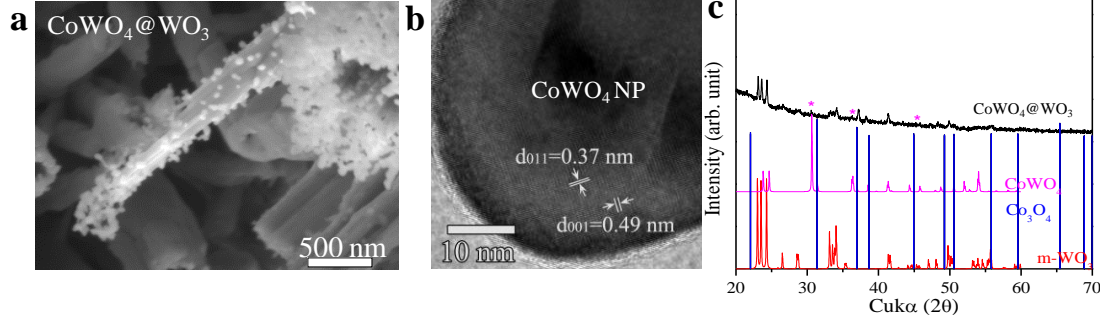
Figure 5.6 (a) SEM, (b) HRTEM image and (c) XRD pattern of $CoWO_4@WO_3$. The HRTEM image and the XRD pattern indicate the formation of monoclinic (wolframite) $CoWO_4$.
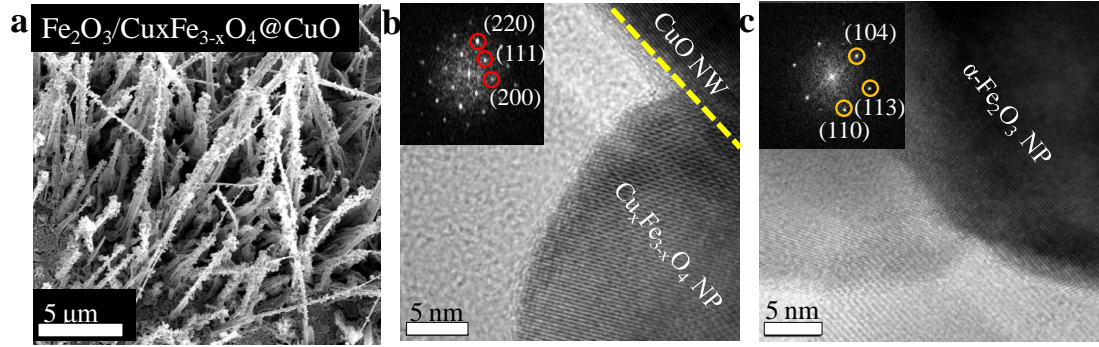
Figure 5.7 (a) SEM and (b, c) HRTEM images of $Fe_2O_3/Cu_xFe_{3-x}O_4@CuO$. The insets of (b) and (c) show the corresponding FFT patterns, which are indexed to spinel structured $Cu_xFe_{3-x}O_4$ and hematite ($\alpha-Fe_2O_3$), respectively. The HRTEM images show that the NPs in direct contact with CuO NW are spinel structured $Cu_xFe_{3-x}O_4$ while those that are not in direct contact with CuO NW are hematite ($\alpha-Fe_2O_3$). This is due to the solid state reaction between CuO and Fe_2O_3 at high temperature.

69

Notably, the sol-flame method can be used to decorate metal oxide NWs with more complicated ternary metal oxide or even noble metal NPs. The ternary oxide NP case is realized by mixing two different metal salt precursors together in the initial sol solution. Specifically, by dip-coating CuO NWs in an Fe and Co salt mixture solution (atomic ratio of Fe:Co is 1:14) and annealing them in a flame, ternary iron-cobalt oxide ($Fe_xCo_{3-x}O_4$, x~0.2) NPs on CuO NW arrays ($Fe_xCo_{3-x}O_4$@CuO) were formed. The TEM image of $Fe_xCo_{3-x}O_4$@CuO (Figure 5.8a) shows that $Fe_xCo_{3-x}O_4$ NPs with an average diameter of 50 nm are uniformly and densely decorated on the CuO NWs with a chain morphology similar to that of the binary metal oxide NPs (Figure 4.4). TEM energy dispersive x-ray spectroscopy (EDS) analysis (Figure 5.8a) shows that the NPs contain uniformly distributed Co and Fe and Cu is mainly contained in the NW core region with a smaller amount exisitng in the NPs as well, indicating that some CuO was dissolved by the acetic acid in the sol-gel solution during the dip-coating process. The formation of $Fe_xCo_{3-x}O_4$ is further confirmed by the SAED patterns for which all the rings are indexed to cubic spinel structure (Figure 5.8b). Similarly, other ternary oxide NPs of $Cu_xCo_{3-x}O_4$ (x~0.2, Figure 5.8c) and $Zn_xFe_{3-x}O_4$ (x~1) were also sucessfully synthesized on CuO NW arrays by the sol-flame method. Significantly, in addition to ternary oxides, Au NPs were decorated onto CuO NWs by the same sol-flame method. As shown in Figure 5.8d, the NPs with an average diameter of 15 nm were uniformly distributed on the surface of the CuO NWs. The ability to decorate ternary oxides and noble metal NPs on NWs greatly increases the chemical tunability and material choice in the final hybrid structured NP@NW, and thus expands their potential application areas.
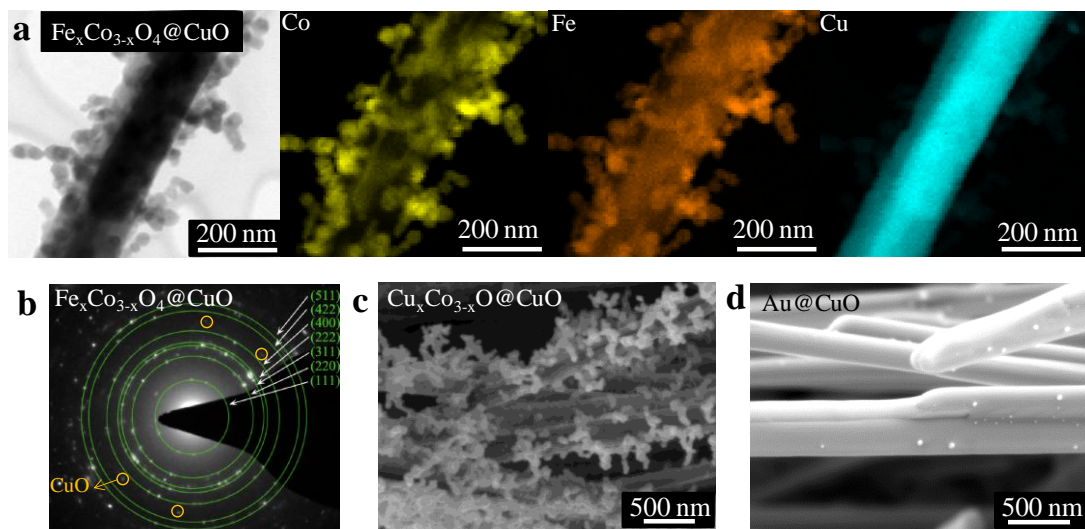
Figure 5.8 (a) TEM image of $Fe_xCo_{3-x}O@CuO$ (x~0.2) NWs and the corresponding TEM-EDS elemental mapping of Co, Fe and Cu. (b) SAED pattern of $Fe_xCo_{3-x}O@CuO$ (x~0.2) NWs and all the ring patterns are indexed to be spinel structure. SEM images of (c) $Cu_xCo_{3-x}O@CuO$ (x~0.2) NWs and (d) Au@CuO NWs, which were also synthesized by the sol-flame method. Effects of flame annealing duration and equivalence ratio on the morphology of NP-chain@NW.

5.3.2. Effects of flame annealing duration and equivalence ratio on the morphology of NP-chain@NW

In Chapter 4, we have shown that the dip-coats layers and the sol precursor concentrations can control both the size and coverage density of the NPs. Here, to complete the study, the effects of flame parameters on the morphology of the hybrid NP-chain@NW structures were also investigated. The same Zn salt-coated CuO NWs were annealed in the flame at different temperatures, for different durations and different flame equivalence ratios (Φ). The morphologies of the final hybrid NP-

71

chain@NW structures are compared in Figure 5.9. First, it should be noted that for the ZnO@CuO structure, the flame annealing temperature, as long as it is above $600^{\circ}C$, has negligible effects on the size and coverage density of the coated ZnO NPs, and the final ZnO NPs always form the chain morphology (Fig. 5.9a and c). Since the sol-gel phase transition temperature of ZnO is $\sim300^{\circ}C$ that is much lower than our observed NP-chain formation temperature, the NP-chain morphology is not caused by the phase change process of the sol-gel solution, but by flame. Second, the flame annealing duration has negligible effects on the morphology of the hybrid NP-chain@NW structure (Figure 5.9c and d). Even a 5 second flame annealing process is sufficient to form the NP-chain structure with high crystallinity, which enables the use of temperature-sensitive delicate substrates (e.g., glass) for the growth of hybrid NWs in flame. Furthermore, the Φ ranging from 0.83 to 1.40 also has little effect on the size, coverage density and uniformity of the NPs (Figure 5.9a and b). Overall, the hybrid NP@NW structure is only sensitive to the flame annealing temperature, not to the flame annealing duration and Φ, which makes the sol-flame method easy to implement with great flexibility.
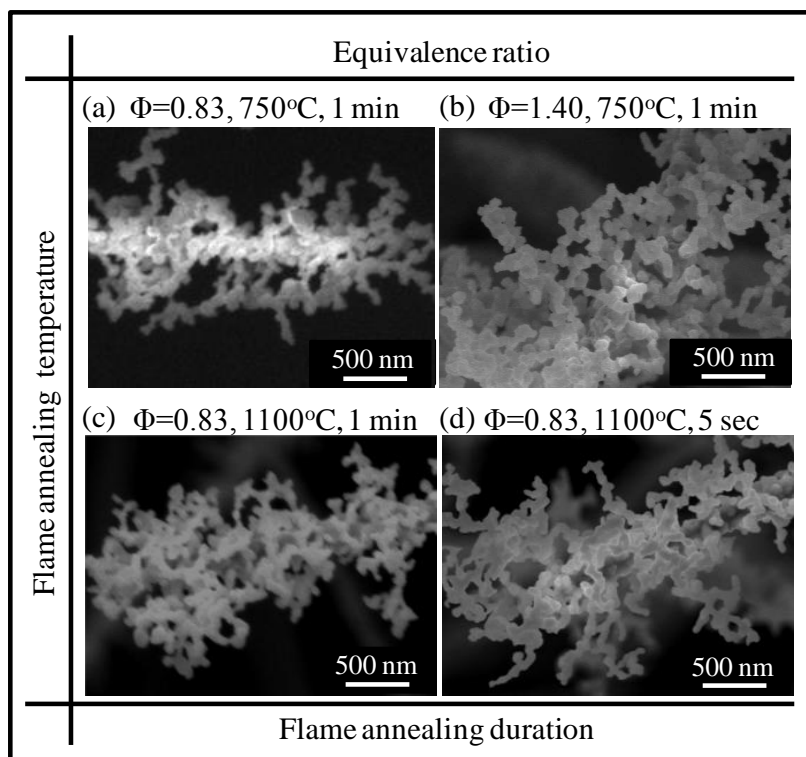
Figure 5.9 SEM images of ZnO@CuO synthesized in different flame conditions which show effects of (a, c) flame annealing temperature, (c, d) flame annealing duration and (a, b) fuel to oxidizer equivalence ratio on the morphology of the NP-chain@NW structure.

5.3.3. NP-shell@NW hybrid structure

Besides the NP-chain@NWs structures, the NP-shell@NWs hybrid structures can also be synthesized by the sol-flame method using lower temperatures (Figure 5.1c). For example, when Zn salt coated CuO NW arrays was annealed by flame at 550°C for 1 min, a uniform ZnO NP shell was formed on the CuO NW surface (Fig. 5.1c), as shown by the transmission electron microscope (TEM, Philips CM20 FEG, 200 kV) image in Figure 5.10. Moreover, the TEM energy dispersive X-ray spectroscopy

analysis (EDS) elemental mapping shows that Cu is concentrated in the 200nm core region, which is the same as the diameter of the bare CuO NWs [117], and Zn is homogeneously distributed over the surface of CuO NW in a 50nm thick shell. Finally, such a hybrid ZnO NP-shell@CuO NW structure was uniformly formed on the entire copper mesh substrate where the CuO NWs were grown initially (Figure 5.1c).
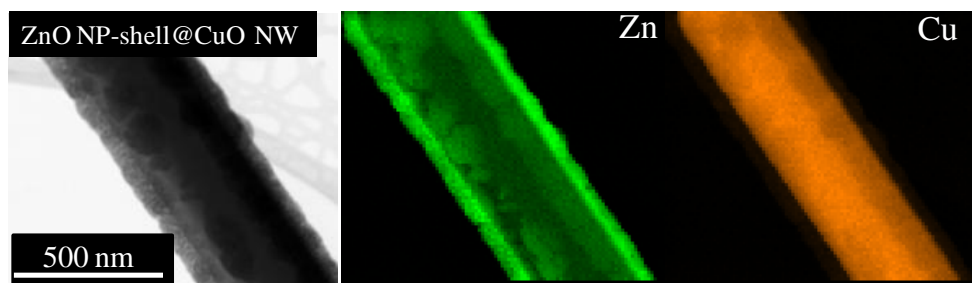
Figure 5.10 TEM image and TEM-EDS elemental mapping of the ZnO NP-shell@CuO NW synthesized by flame annealing Zn salt-coated CuO NW at 550°C for 1 min.

5.3.4. *Doped NW hybrid structures*

Besides coating NWs with NP shells or chains, the sol-flame method is also a simple but powerful method to dope NWs. Incorporating dopants into materials is a common way to modify their electrical and optical properties. For example, anion-doped TiO_2 exhibited improved optical and electrical properties and hence enhanced performance for PEC water splitting and photocatalysis [125, 130, 131]. Many existing doping methods, such as hydrothermal [125, 131], sol-gel [132] and impregnation [133], incorporate dopants during the growth (in-situ doping), which can negatively impact the crystallinity of the final materials and change their morphology

74

[125, 133]. The sol-flame method, instead, introduces dopants into existing NW crystals (ex-situ doping), so it minimizes the structural disadvantages of dopants and maintains the original crystallinity of the starting materials. To demonstrate the doping capability of the sol-flame method (Figure 5.1e), we first synthesized TiO_2 NW arrays on fluorine-doped tin oxide (FTO) substrates by hydrothermal method [126] (supplemental material 1), and then dip-coated the FTO substrates with a tungsten salt solution prepared by the sol-gel method. After drying in air, the W salt-coated TiO_2 NWs were annealed in the flame at 1100^oC for 1 min. It should be noted that such brief exposure to the flame did not damage the delicate FTO substrate for which the safe temperature is ordinarily below 550^oC. For comparison, the same W-coated TiO_2 NWs were annealed in a tube furnace at 550^oC for 1 h, which is the normal temperature and duration to treat oxides grown on the FTO substrate due to the risk of damaging the FTO at higher temperature. The morphologies of the as-grown (Figure 5.11a), flame-annealed (Figure 5.11b and 5.1e) and furnace-annealed (Figure 5.11c) TiO_2 NW arrays are compared in Figure 5.11. First, the as-grown and flame-annealed TiO_2 NWs have almost identical morphology, with dense and well-aligned TiO_2 NWs on the FTO substrate and an average diameter of 100nm. Next, the doping quality of the flame-annealed TiO_2 was clearly shown by the TEM-EDS elemental mapping (Figure 5.12), which shows that W, similar to Ti, is uniformly distributed in the entire NW. Nevertheless, for the furnace-annealed TiO_2 NW arrays, some WO_3 particles (Figure 5.11c, shown in circles) are formed on the surface of TiO_2, since there is lack of energy for W atoms to diffuse into the TiO_2 at such a low temperature, so the normal furnace annealing is not effective in doping materials without damaging the

75

substrate. These results indicate that the high temperature and short duration of flame annealing are very effective to facilitate the dopant diffusion into existing crystal structures without changing the morphology of the original materials and damaging delicate substrates.

(a) As-grown TiO$_2$

(b) W-doped TiO$_2$ (flame)

(c) W-doped TiO$_2$ (furnace)

TiO$_2$

WO$_3$ NPs

FTO

1 µm   1 µm   1 µm
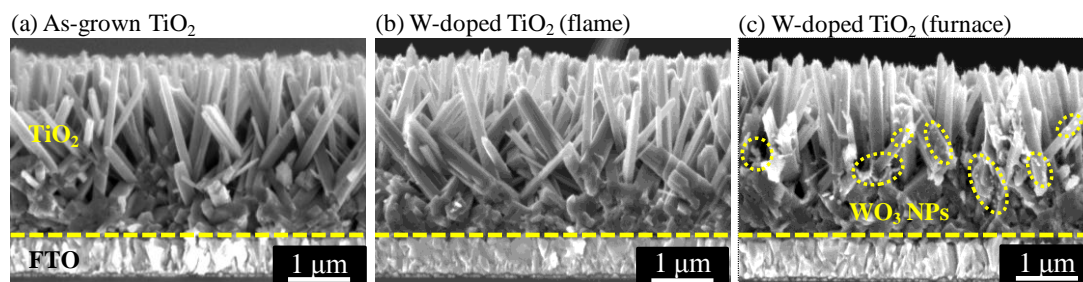
Figure 5.11 SEM images of (a) as-grown TiO$_2$ NW arrays and W doped TiO$_2$ NW arrays by annealing W salt-coated TiO$_2$ NW in (b) flame at 1100°C for 1 min and (c) furnace at 550°C for 1 h, with the formation of WO$_3$ NPs as circled.

W-doped TiO$_2$ Ti   W

100 nm
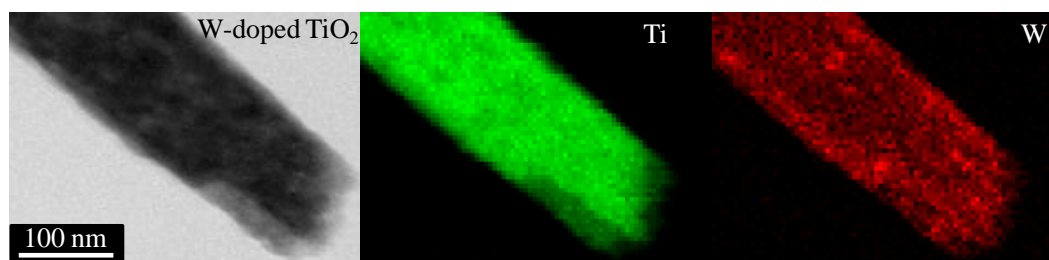
Figure 5.12 TEM image and TEM-EDS elemental mapping of W doped TiO$_2$ NW synthesized by flame annealing W salt-coated TiO$_2$ NWs at 1100°C for 1 min.

5.4. Conclusion

In summary, with the sol-flame method, we have successfully synthesized three different types of hybrid metal oxide NWs, including NP-shell@NW, NP-chain@NW, and doped NWs. First, for both the NP-shell@NW and NP-chain@NW cases, the NP

morphology is mainly determined by the flame annealing temperature and has little dependence on the flame annealing duration and equivalence ratio. When the flame annealing temperature is high enough to ignite the remaining solvent in the metal salt shell, the NP forms the chain morphology. Second, for both the NP-shell@NW and NP-chain@NW cases, compared to furnace annealing in air, the ultrafast heating rate and the high temperature of flame enable rapid solvent evaporation/combustion and nucleation of NPs in the vicinity of the NWs, leading to higher loading density of NPs with smaller sizes. Finally, for doped NWs, the high temperature flame enables rapid and efficient dopant diffusion, even with a brief annealing duration that protects the original materials and substrates from damage. Given the advantages and generality of the sol-flame process, we believe it can be applied to synthesize various 1-D hybrid metal oxide nanostructures, and thereby impact diverse application areas.

Chapter 6. Cu^{2+} Enhanced Synthesis of Co_3O_4 NWs for CH_4 Oxidation

6.1.   Introduction

Chapter 2 to 5 have stated the catalytic activity of CuO NWs based system, and shown the advantages of the 1-D metal oxide nanocatalysts supported on metal meshes. In Chapter 5, as the most active metal oxide catalyst, Co_3O_4 was introduced to our study to increase the catalytic activity of the CuO NWs. In this chapter, Co_3O_4 NWs will be studied, and Co and Cu will be incorporated in situ. Specifically, the Co_3O_4 NWs will be synthesized with the existence of Cu.

Despite the fact that Co_3O_4 is the most active catalyst among all the transition metal oxides for the oxidation of CO and hydrocarbons in general [118], the controllable synthesis of 1-D nanostructured Co_3O_4 on metal meshes remains a challenge. 1-D Co_3O_4 NWs have recently been synthesized on Si wafers, polystyrene substrates [134] and Ti foils [135] by Li et al. using the ammonia-evaporation-induced synthesis method which, in principle, enables the fabrication of 1-D Co_3O_4 on metal meshes. The same synthesis method was adopted by Marban et al. [67] to grow Co_3O_4 NWs on stainless steel (SS) mesh substrates to yield a highly active and stable catalyst for the preferential oxidation of CO. However, this ammonia-evaporation-induced synthesis method depends heavily on the evaporation rate of ammonia, which, in turn, is very sensitive to the ambient oxygen partial pressure in the reaction bath and small

78

temperature fluctuations. Consequently, the synthesis method has poor repeatability, and the Co_3O_4 NWs sometimes have poor uniformity and low surface coverage density [67, 135].

It has been reported for solution phase synthesis that the morphology of the final products can be controlled by adding other metal ions in the initial aqueous solution [136-138]. Herein, we introduced Cu^{2+} ions in the ammonia-evaporation-induced growth method to control the morphology and to increase the surface coverage density of the 1-D Co_3O_4 synthesized on SS mesh. The catalytic activities of the Co_3O_4 grown by the original and improved synthesis methods were compared for the methane (CH_4) oxidation reaction. The results show that the Cu^{2+} ion greatly improves the mass loading and coverage density of Co_3O_4 nanostructures on the SS mesh substrate, leading to higher catalytic activity.

The 1-D Co_3O_4 structures were synthesized by a method based on the ammonia-evaporation-induced synthesis originally reported by Li et al. [134], but with the addition of precursors containing Cu^{2+} ions (see Experimental Section). The Co_3O_4 samples are named $Co_3O_4\_Cu0$, $Co_3O_4\_Cu1$, $Co_3O_4\_Cu2$ and $Co_3O_4\_Cu5$, respectively, based on the initial amount of Cu^{2+} ions added to the aqueous solution.

6.2. Experimental Specifications

In a typical synthesis, a fixed amount of 8 mmol $Co(NO_3)_2•6H_2O$ with different amounts of $Cu(NO_3)_2•4H_2O$ (0, 1, 2 or 5 mmol) were firstly dissolved in an aqueous solution containing deionized (DI) water (20 ml) and 30% wt. ammonia (30 ml) to form a clear solution. The solution was magnetically stirred for 10 min in air and

subsequently transferred to a beaker (100 ml capacity). A piece of SS mesh (0.0045"
wire diameter and 0.0055" opening size, McMaster) was placed at the bottom of the
beaker as the growth substrate. The beaker with the mixture was then covered by a
glass slide and kept in an oven at 90°C for 12 h for the growth of 1-D Co_3O_4
nanostructures. After the growth, the SS mesh substrate was thoroughly washed with
DI water and dried in air. Finally, the substrate was annealed in air at 250°C for 3 h.

All the Co_3O_4 samples used for the catalytic test were grown on pieces of SS
mesh with identical dimensions of 3" $\times$ 12", which was rolled up to a 3" long and 0.7"
diameter cylinder to fit into a 1" diameter quartz tube in a home-built tube flow reactor
with details reported previously [85, 117]. The inflow was a mixture of 1.5% vol. CH_4
and 6.0% vol. O_2 diluted in He with a total flow rate of 100 sccm, and the flow rate of
each gas was controlled by mass flow controllers (MFC, Z500, Horiba). The
composition of the effluent gas was analyzed by a gas chromatograph (GC, SRI
Multiple Gas Analyzer #3 on the 8610C chassis equipped with a thermal conductivity
detector and a Hayesep-D column). During the catalytic tests, all the samples stayed
well attached to the SS substrate and no peeling off was observed.

6.3.   Results and Discussion

6.3.1. Materials characterization

The scanning electron microscope (SEM, FEI XL30 Sirion, 5kV) images of the
Co_3O_4_Cu0 (Figure 6.1a, b), Co_3O_4_Cu1 (Figure 6.1c, d), Co_3O_4_Cu2 (Figure 6.1e, f)
and Co_3O_4_Cu5 (Figure 6.1g, h) clearly show that with the increase of Cu^{2+} ion

concentration in the initial aqueous solution, the surface coverage of Co_3O_4 structures on the SS mesh becomes denser and more uniform. Moreover, the initial Cu^{2+} ion concentration also affects the final morphology of Co_3O_4, which varies from NW bundles (Figure 6.1b) to single microwires (MWs) (Figure 6.1d, f), to MWs with a surface coating (Figure 6.1h). It should be noted that even for the Co_3O_4_Cu0 case, we obtained NW bundles instead of single NWs produced by the same method in another study [134], indicating the sensitivity of the original ammonia-evaporation-induced synthesis method to the experimental environment. Among the nanostructures grown with the four Cu^{2+} ion concentrations tested, the Co_3O_4_Cu2 MWs (Figure 6.1e, f) have the optimal coverage density and morphology, and are about 40 μm long, much longer than Co_3O_4 NWs grown on Si wafers (15 μm) [134] and on SS wire meshes (30 μm) [67] with similar growth conditions and duration using the unmodified ammonia-evaporation-induced method. The morphology change observed in Figure 6.1 strongly indicates that the introduction of Cu^{2+} ions in the synthesis process facilitates the nucleation of the solid Co_3O_4 phase, and thus affects the growth uniformity and surface coverage density of the Co_3O_4 MWs on SS meshes. Importantly, the growth of 1-D Co_3O_4 structures on SS meshes with Cu^{2+} ion addition is very repeatable.

The mass loadings and surface areas of the Co_3O_4 structures with different amounts of Cu^{2+} ion addition are quantitatively compared and listed in Table 5.1. The mass loading density of the Co_3O_4_Cu0 on SS mesh is about 8.0 mg/cm^2, which is more than three times higher than the 2.3 mg/cm^2 for the mesoporous Co_3O_4 NWs grown on Ti foils by Li et al. [135] and comparable to the 7.0 mg/cm^2 for the Co_3O_4 NWs grown on similar SS mesh reported by Marban et al. [67]. In addition, despite

the fact that our $Co_3O_4\_Cu0$ structures, are NW bundles and not separate, individual NWs, their Brunauer-Emmett-Teller (BET) surface area is about 70 m^2/g (Table 5.1), comparable to the previously reported 74 m^2/g for NWs on Ti foils [135] and 71 m^2/g for NWs on SS meshes [67], which indicates that our MWs might have nanosized features such as mesoporous structures and small grain sizes. More importantly, when Cu^{2+} ions are added to the initial solution, the mass loading densities of Co_3O_4 are increased from 8.0 mg/cm^2 to around 10~12 mg/cm^2 on SS mesh (Table 5.1). Correspondingly, the specific surface area is also increased, with the highest 79 m^2/g for $Co_3O_4\_Cu2$ due to its optimized morphology. The quantified measurement of both loading density and specific surface area increase reconfirms that the Cu^{2+} ion can promote the nucleation and growth of Co_3O_4 on SS mesh, as shown in Figure 6.1.
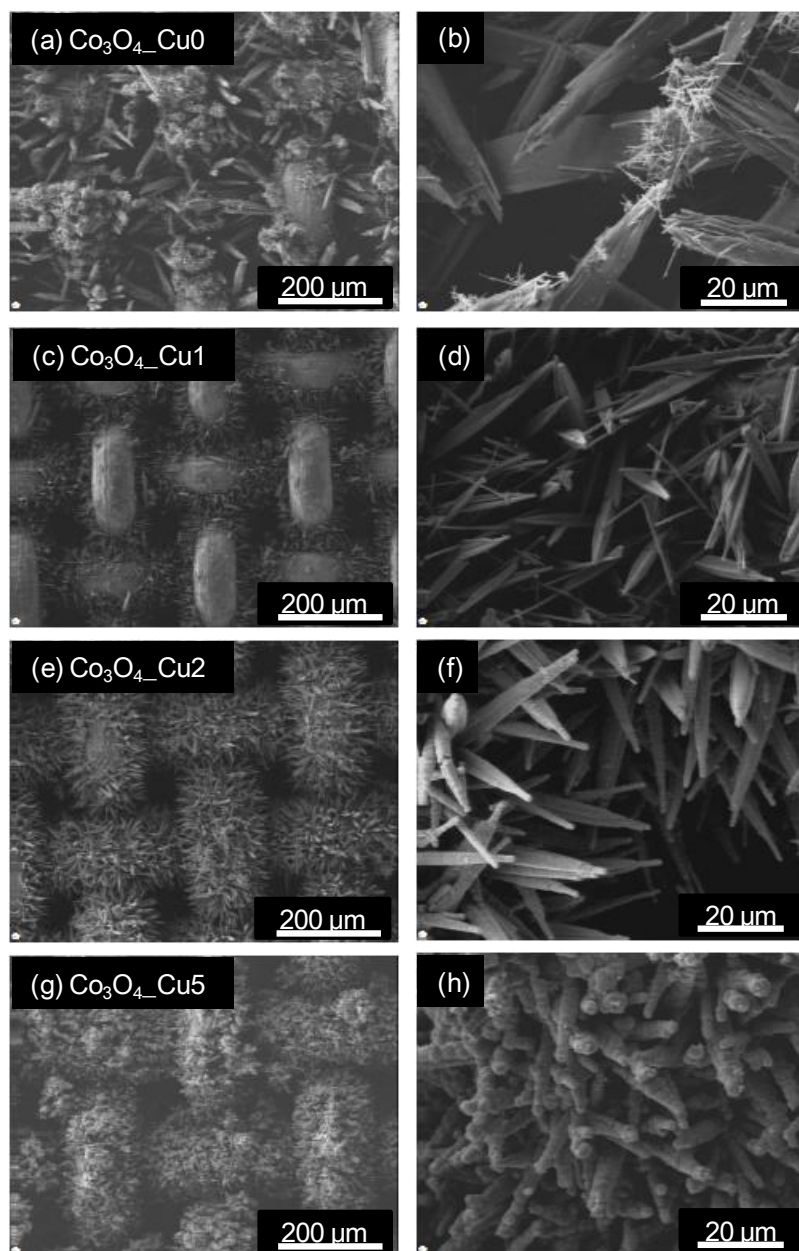
Figure 6.1 SEM images of (a, b) $Co_3O_4\_Cu0$, (c, d) $Co_3O_4\_Cu1$, (e, f) $Co_3O_4\_Cu2$ and (g, h) $Co_3O_4\_Cu5$.

The chemical compositions of the Co_3O_4 samples were systematically analyzed by various characterization methods. The parallel beam X-ray diffraction (XRD, PANalytical XPert 2, 45 kV, 40 mA) patterns of $Co_3O_4\_Cu0$, $Co_3O_4\_Cu2$ and

$Co_3O_4\_Cu5$ (Figure 6.2a) show that the main phase of all three samples is the Co_3O_4 spinel phase with no CuO phase detected. However, since the mixed $Co_{3-x}Cu_xO_4$ oxides (e.g., $Cu_{0.92}Co_{2.08}O_4$, $Cu_{0.76}Co_{2.24}O_4$) are also spinel phases and have almost identical lattice parameters with those of Co_3O_4, the XRD pattern alone cannot exclude the possible existence of the mixed $Co_{3-x}Cu_xO_4$. Energy dispersive X-ray spectroscopy (SEM-EDS, 15kV) was taken to further determine if Cu is incorporated in the optimal $Co_3O_4\_Cu2$ MWs, and the elemental mapping (Figure 6.3) clearly shows that the MWs contain both Co and Cu. The presence of Cu in the Co_3O_4 structures is further confirmed by an inductively coupled plasma mass spectrometry (ICP-MS, Thermo Scientific XSERIES 2) measurement. For $Co_3O_4\_Cu1$, $Co_3O_4\_Cu2$ and $Co_3O_4\_Cu5$, the mass percentage of Cu in the final solid product on the SS mesh is 1.2%, 1.6% and 3.2%, respectively. Finally, surface sensitive X-ray photoelectron spectroscopy (XPS, SSI S-Probe, monochromatized Al kα radiation at 1486 eV) analysis shows that the amount of surface Cu is below 0.3%. Therefore, we believe that the most of Cu is present in the bulk region, and not at the surface, of the MWs. In other words, the surface of all the Co_3O_4 samples is mainly covered by Co_3O_4 and the catalytic property is therefore mainly just that of Co_3O_4.
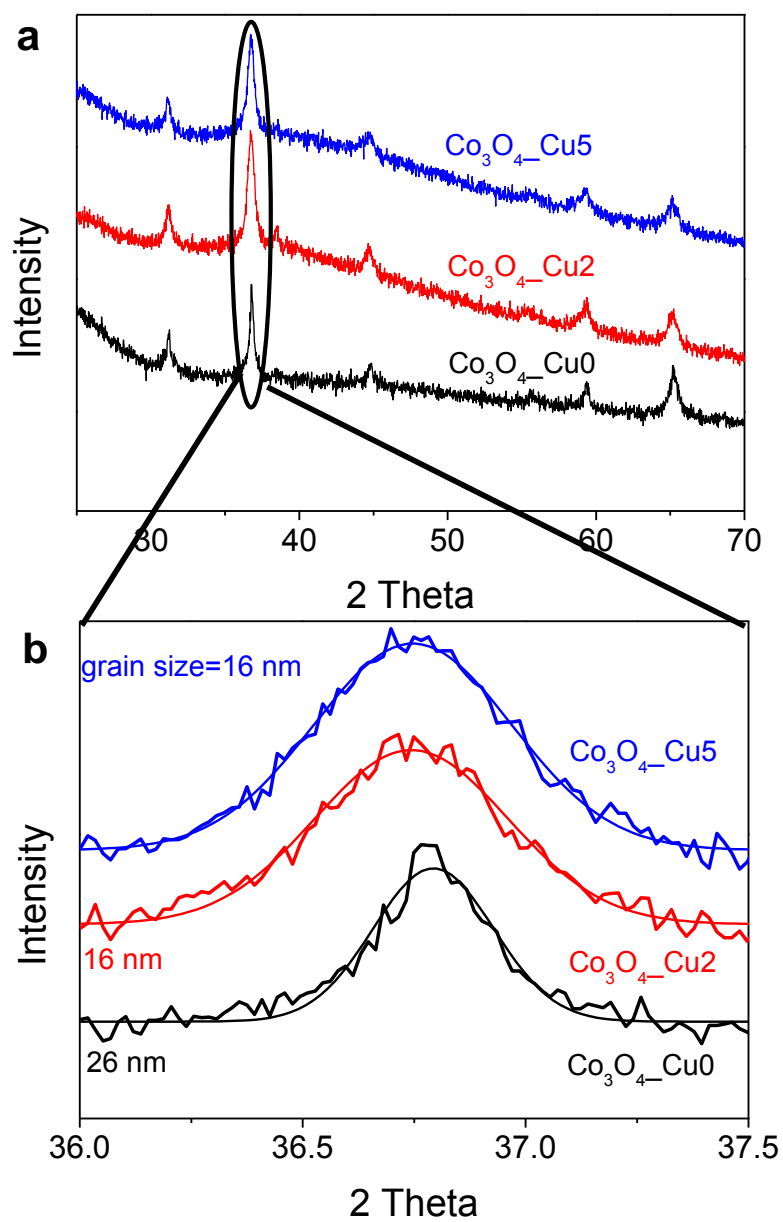
Figure 6.2 (a) X-ray diffraction pattern of $Co_3O_4\_Cu0$, $Co_3O_4\_Cu2$ and $Co_3O_4\_Cu5$ and (b) the Gauss fitting of the main peaks.
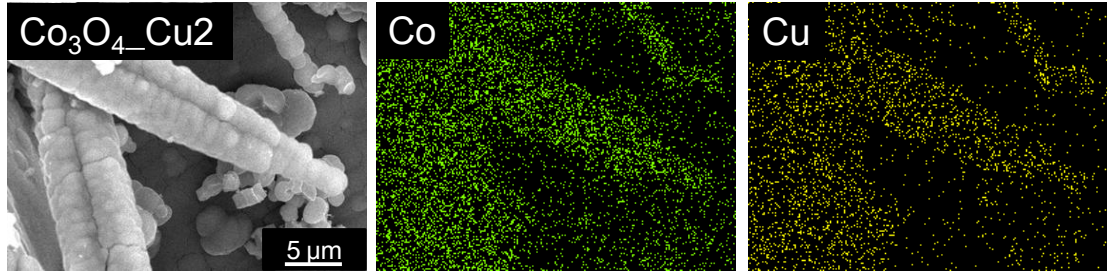
Figure 6.3 SEM images of $Co_3O_4\_Cu2$ with EDS elemental mapping of Co and Cu.

6.3.2. Growth mechanism

Based on the observations above, the growth mechanism of Co_3O_4 with/without Cu is proposed and illustrated in Figure 4. Without the presence of Cu^{2+} ions, only $Co(OH)_2$ nucleates on the SS mesh though the following reaction (5.1).

$$Co(NH_3)_6^{2+}(aq) + 2\,OH^-\,(aq) \xrightarrow{90°C} Co(OH)_2\,(s) + 6\,NH_3\,(g) \qquad (5.1)$$
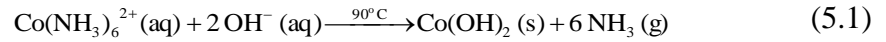
Typically, after 2 h of growth, only a small number of nuclei are sparsely deposited on the SS mesh, as shown in the left SEM image in Figure 6.4a. $Co(OH)_2$ further deposits on the nuclei to form NW or NW bundles, driven by a screw dislocation [139]. After annealing in air, $Co(OH)_2$ is oxidized to the product Co_3O_4 (Figure 6.1a, b). However, when Cu^{2+} ions are present in the initial solution, Cu^{2+} will also react with OH^- through a similar reaction (5.2).

$$Cu(NH_3)_4^{2+}\,(aq) + 2\,OH^-\,(aq) \xrightarrow{90°C} Cu(OH)_2\,(s) + 4\,NH_3\,(aq) \qquad (5.2)$$
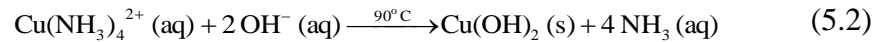
In other words, both $Cu(OH)_2$ and $Co(OH)_2$ will nucleate on the SS substrate. Nevertheless, $Cu(OH)_2$ has a much smaller solubility product constant ($k_{sp}=10^{-19.66}$) than does $Co(OH)_2$ ($k_{sp} = 10^{-14.32}$) [140], so $Cu(OH)_2$ has a stronger tendency to

86

nucleate. As a result, when Cu^{2+} ions are present in the initial solution, the density of nuclei on the substrate is much higher than that in the case without Cu^{2+} ions after 2 h of growth, and almost the entire surface of the substrate is covered by the nuclei (Figure 6.4b, left SEM image). The fact that the presence of Cu^{2+} ion promotes nucleation is also supported by examining the loose, unattached solid precipitates in the reaction bath, since increasing the concentration of Cu^{2+} ion promotes not only the nucleation of solid structures on the SS mesh but also in the solution.

a. Without Cu²⁺ ions

Nuclei on the substrate   Precipitates in the reaction bath
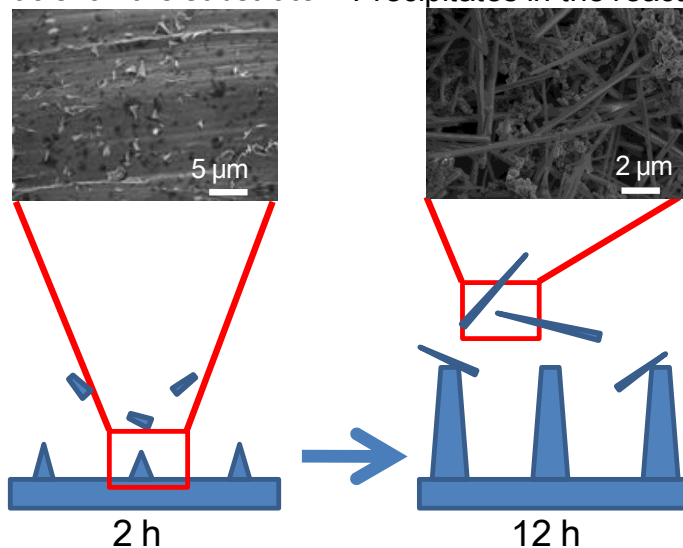
5 µm   2 µm

2 h   12 h

b. With Cu²⁺ ions

Nuclei on the substrate   Precipitates in the reaction bath

5 µm   2 µm

2 h   12 h

● $Cu(OH)_2$ nuclei   ◢ $Co(OH)_2$ nuclei
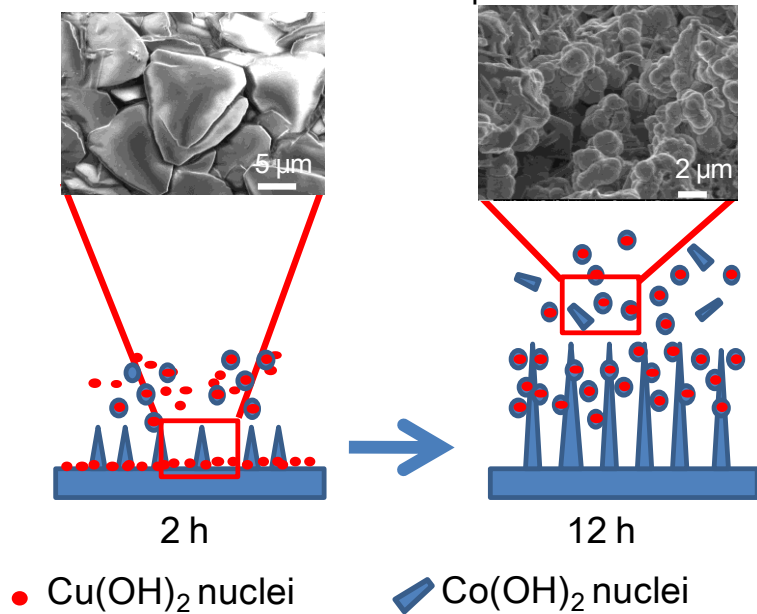
Figure 6.4 Growth mechanism of Co_3O_4 structures (a) without and (b) with Cu^{2+} ions in the initial solution. The inset SEM images showed the morphologies of the corresponding regions

After 12 h of growth in the absence of Cu^{2+} ion, single NWs were the main loose precipitate (Figure 6.4a, right SEM image), but in the presence of Cu^{2+} ion, particle precipitates were also found (Figure 6.4b, right SEM image). When the initial concentration of Cu^{2+} ion is too high, the morphology of Co_3O_4 on SS mesh changes to surface coated MWs (Figure 6.1f) since the nucleation on the sidewall of MWs is also enhanced. Hence, an optimal amount of Cu^{2+} exists for maximizing the surface area of the Co_3O_4 structures to promote nucleation while avoiding excessive surface coating. Finally, the grain sizes of the Co_3O_4 structures are also affected by the Cu^{2+} ion. The grain sizes for $Co_3O_4\_Cu0$, $Co_3O_4\_Cu2$ and $Co_3O_4\_Cu5$ calculated by the Scherrer Equation are 26 nm, 16 nm and 16 nm, respectively (Figure 6.2b). This is consistent with the specific surface areas of the samples (Table 6.1) and also confirms that the Cu^{2+} ions in the solution participate in the growth process. These observations illustrate the effectiveness and simplicity of controlling the morphology and coverage density of 1-D Co_3O_4 by adding different amounts of Cu^{2+} ions in the synthesis process.

6.3.3. *Catalytic activity for CH₄ oxidation*

The catalytic activities of the $Co_3O_4\_Cu0$, $Co_3O_4\_Cu1$, $Co_3O_4\_Cu2$ and $Co_3O_4\_Cu5$ samples were further compared for the methane (CH_4) oxidation reaction as shown in Figure 6, where the conversion percentage of CH_4 is defined as

$$CH_4\% = \frac{X_{CH_4}(\text{initial}) - X_{CH_4}(\text{exhausted})}{X_{CH_4}(\text{initial})}$$

, where X_{CH4}(initial) and X_{CH4}(exhausted) are the mole fractions of CH_4 in the initial and exhausted gases, respectively. The detected products by gas chromatograph consist of CO_2 and H_2O with no CO detected, so methane has been fully oxidized. First, it can be seen that the CH_4 conversion percentages over the all the Cu-containing Co_3O_4 samples are higher than that over Co_3O_4_Cu0 for the entire temperature range of 300-600°C. Second, the CH_4 conversion percentage peaks over Co_3O_4_Cu2 (Figure 6.5), with about 10 to 25% higher conversion than that of the Co_3O_4_Cu0 case depending on the temperature. Finally, when the CH_4 conversion percentage is normalized by the surface area of catalysts, the reaction rate per unit area of catalyst is very similar for the three Cu-containing Co_3O_4 samples and the Co_3O_4_Cu0 sample (Table 5.1), indicating that all the surfaces are mainly covered by Co_3O_4 with similar chemical properties. However, when the reaction rate of CH_4 is normalized by the mass of the catalysts (without counting the substrate mass, Table 5.1), all the Cu-containing Co_3O_4 samples, especially the Co_3O_4_Cu2 sample, exhibit higher catalytic activity, which is a consequence of their larger specific surface areas. These results illustrate the benefit of introducing the Cu^{2+} ion to the synthesis, which enables higher catalyst loading on the same supporting SS mesh and, hence, higher CH_4 conversion percentage. The stability tests of the Co_3O_4_Cu0 and Co_3O_4_Cu2 samples at 600°C were also performed (Figure 6.6). The results showed that the Co_3O_4_Cu2 sample has both higher activity and better stability than those of the pure Co_3O_4_Cu0 sample [141].
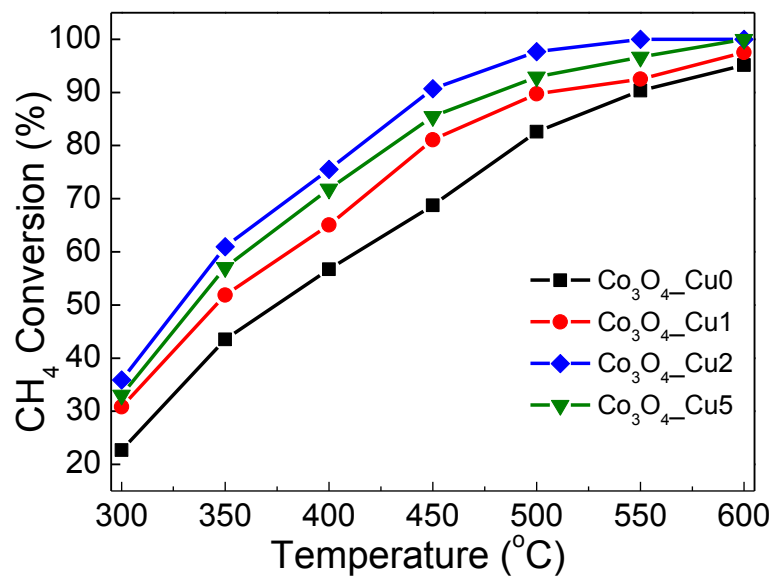
Figure 6.5 Methane conversion percentages over $Co_3O_4\_Cu0$, $Co_3O_4\_Cu1$, $Co_3O_4\_Cu2$ and $Co_3O_4\_Cu5$ in the temperature range of 300 to 600^oC. The inflow gas is 1.5% vol. methane and 6.0% vol. oxygen balanced in Helium, with a total flow rate of 100 sccm.
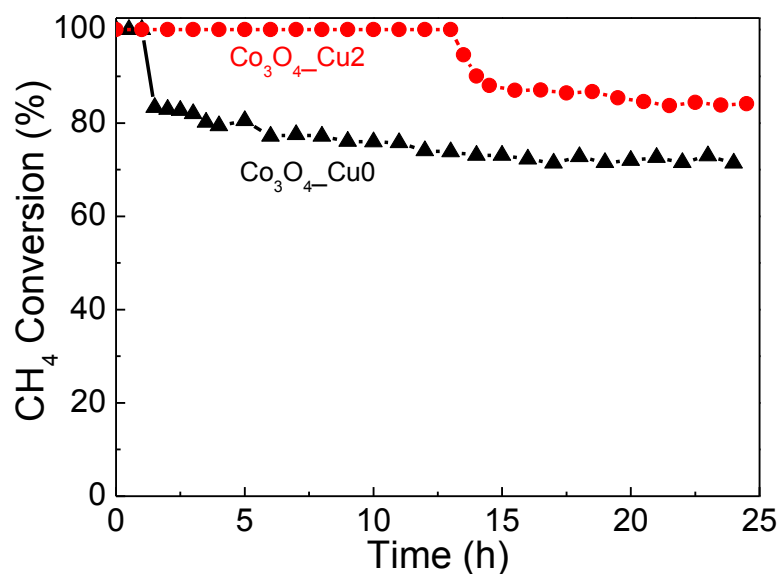
Figure 6.6 Methane conversion over the Co_3O_4_Cu0 and Co_3O_4_Cu2 samples at 600°C for 24 h. The inflow gas was 1.5% vol. methane and 6.0% vol. oxygen balanced in Helium, with a total flow rate of 100 sccm.

Table 6.1 Comparison of Co_3O_4 samples with various amounts of Cu^{2+} ion addition. The methane conversion rate is calculated at 300 °C.

Sample	Mass loading density (mg/cm^2)	S (m^2/g) (without substrate)	$R*10^6$ (mol/m^2*s) per unit area of catalyst	$R*10^4$ ($mol/g*s$) per unit mass of catalyst
Co3O4_Cu0	8.0	70	2.10	1.46
Co3O4_Cu1	10.1	71	2.19	1.55
Co3O4_Cu2	10.7	79	2.16	1.70
Co3O4_Cu5	11.1	70	2.14	1.50

6.4. Conclusion

In summary, we synthesized 1-D nanostructured Co_3O_4 catalyst on SS mesh with a simple and improved ammonia-evaporation-induced synthesis method, which introduces Cu^{2+} ion to facilitate the nucleation and growth process of $Co(OH)_2$. Firstly, with Cu^{2+} ions present in the initial solution, the morphology of Co_3O_4 evolves from NW bundles to MWs, and finally to surface-coated MWs. Secondly, the introduction of Cu^{2+} ions increases the mass loading density of Co_3O_4 on SS meshes. There exists an optimal amount of Cu^{2+} ion addition that maximizes the specific surface area of Co_3O_4. Finally, with smaller grain sizes and larger surface areas, all the Cu-containing Co_3O_4 samples exhibit higher catalytic activity for CH_4 oxidation than the pure Co_3O_4. We believe that these results not only demonstrate an elegant method to control the morphologies of 1-D metal oxides synthesized by solution phase methods, but also facilitate the use of 1-D metal oxide nanocatalysts supported on metal mesh as an economical, scalable and yet efficient catalytic structure for hydrocarbon oxidation reactions and other catalytic applications.

Chapter 7.   Conclusion and Recommendations for Future Work

7.1.   Conclusion

This thesis presents our research in catalytic properties, modification and decoration of metal oxide NWs for hydrocarbons oxidation.

The catalytic oxidation of hydrocarbons process is essential for minimizing emissions of pollutants and utilizing the fuel. Nanostructured metal oxide catalysts hold the merits of abundant supply, large surface area and high thermal stability.

1-D nanostructured metal oxides on metal mesh substrates have been used as catalysts for hydrocarbons oxidation. There are several benefits of the 1-D nanostructured catalysts. First, these catalysts avoid the aggregation problem for the conventional supported nanoparticles (NPs) catalysts, due to the strong adhesion to the substrate, therefore, the catalytic activity can be easily increase by increasing the loading of nanowires (NWs). Second, the use of the metal substrates reduces the interactions between the catalysts and the substrates, which may reversely affect the activity; it also simplifies the system, which provides a good platform for fundamental study. Moreover, the surface of the 1-D nanostructured catalysts is exposed instead of embedding in supports, leading to convenience in tuning the surface chemistry for higher catalytic activity. Therefore, the 1-D nanostructured metal oxides are promising catalysts, in both fundamental study and application.

We have grown CuO NWs on Cu mesh, which is one of the most active metal oxide catalysts, and have demonstrated that the CuO NWs are promising catalysts for

CH_4 oxidation due to their simplicity and low cost in synthesis, notable stability in operation, suitability for *in situ* regeneration, flexibility in loading variation, and most importantly, comparable catalytic activities to those of supported CuO NPs. Our kinetic analysis have shown that the oxidation rate of CH_4 has a nearly linear dependence on the CH_4 concentration but a weak dependence on the O_2 concentration, so the oxidation step of CH_4 by the surface oxygen is likely to be the rate determining step.

To further increase the catalytic activity of the CuO NWs, we have applied two methods. The first one is to briefly treat the CuO NWs with Ar or H_2 RF plasma. The CO oxidation percentage has been increased from 24% over CuO_as_grown NWs to 29% and 85% over CuO_Ar_RF and CuO_H$_2$_RF NWs respectively at 140^oC in the fuel lean condition, and similar level of improvement has been observed for the fuel rich condition as well. The enhancement from the plasma treatment is caused by the creation of grain boundaries and the reduction of Cu(II) to the more active Cu(I). The kinetic study has shown that the bulk oxygen in CuO NWs also participates in the catalytic oxidation of CO, and the diffusion rate of bulk oxygen to surface is higher in CuO_H$_2$_RF NWs, which could be one of the reasons for higher activity of Cu_2O than that of CuO.

The second tuning method was to decorate the CuO NWs with more active NP materials, Co_3O_4 NPs, with a newly developed simple, fast and general sol-flame method. After the Co_3O_4 decoration, the CuO NWs surface was uniformly and densely covered by Co_3O_4 NP-chain structures, which offered large NP loading, high surface

area and minimal aggregation, resulting in times higher catalytic activity for CH_4 oxidation reactions than the bare CuO NWs.

In addition, this sol-flame method is a general method to decorate NWs with various NPs, and even to dope NWs with dopants for desirable properties. We have successfully synthesized a range of NP-chain decorated NWs (NP-chain@NW), NP-shell coated NWs (NP-shell@NW) and doped NWs, such as TiO_2@CuO, ZnO@WO_3, ZnO@CuO, Au@CuO and W-doped TiO_2 NWs using this method. These hybrid NWs have shown promising properties in various application fields.

Moreover, to incorporate Co and Cu and study the synergetic effects, we have synthesized 1-D nanostructured Co_3O_4 catalyst on SS mesh with the introduction of Cu^{2+} ion to facilitate the nucleation and growth process of $Co(OH)_2$. Firstly, with Cu^{2+} ions present in the initial solution, the morphology of Co_3O_4 evolves from NW bundles to MWs, and finally to surface-coated MWs. Secondly, the introduction of Cu^{2+} ions increases the mass loading density of Co_3O_4 on SS meshes. There exists an optimal amount of Cu^{2+} ion addition that maximizes the specific surface area of Co_3O_4. Finally, with smaller grain sizes and larger surface areas, all the Cu-containing Co_3O_4 samples exhibit higher catalytic activity for CH_4 oxidation than the pure Co_3O_4. We believe that these results not only demonstrate an elegant method to control the morphologies of 1-D metal oxides synthesized by solution phase methods, but also facilitate the use of 1-D metal oxide nanocatalysts supported on metal mesh as an economical, scalable and yet efficient catalytic structure for hydrocarbon oxidation reactions and other catalytic applications.

This thesis has shown that the 1-D metal oxide on metal mesh catalysts are good alternative to the conventional supported NPs. These 1-D nanostructured catalysts exhibit comparable or even better catalytic activity and stability, great flexibility in increasing the catalyst loading, and convenience in tuning the surface chemistry. We believe these benefits of the 1-D catalysts can impact the catalysis and other related application fields.

7.2. Recommendations for future work

7.2.1. 1-D nanostructured catalysts for large hydrocarbons oxidation

The current state of the 1-D nanostructured metal oxide catalysts is in a fundamental study and feasibility exploration phase. There is no doubt that the 1-D catalysts are an alternative of the supported NP catalysts, and exhibit advantages in some application and research fields over the supported NPs. Nevertheless, so far, the hydrocarbon used in this study is limited to methane, which is the simplest hydrocarbon and in gas phase. Since the fuels used most widely are large hydrocarbons in liquid phase, the application of 1-D nanocatalysts in liquid fuels, including the dispersion, stability, recycling and catalytic properties can be further considered and studied.

In addition, for industrial application, the study of large scale synthesis of the 1-D nanostructured metal oxides and the integration of the catalysts to the existing catalytic system is also needed.

7.2.2. Complex metal oxide NWs catalysts

It is known that the metal oxides are promising catalysts for the abundance, low cost and high stability [19], though the activity is lower compared to the noble metals. This thesis has discussed several methods to increase the catalytic activity of 1-D nanostructured metal oxides; however, it is limited to binary oxides, or combination of binary oxides. It is reported that the complex metal oxides, such as the perovskite structured metal oxides, show higher catalytic activity than that of the binary ones, especially when carefully engineered the dopants [20, 28, 142, 143]. Nevertheless, the general synthesis of pervoskite metal oxide NWs on metal mesh substrates remains a challenge [144]. The previous methods are based on solution processes, normally with templates and toxic/unstable organometallic precursors, resulting in small yields and narrow materials choice.

The general fabrication procedure of 1-D nanostructured pervoskite metal oxide catalysts, especially the non-template methods, is worth study. Direct growth on metal mesh and facet structures are preferred. After the growth, the catalytic properties and further modification/decoration can also be investigated.

7.2.3. Fundamental studies of sol-flame method

Chapter 5 and 6 have shown that the sol-flame method enables the synthesis of hybrid NWs, including the hierarchical NWs, core/shell NWs and doped NWs, which are promising materials in many application fields, such as supercapacitors, lithium ion batteries, photoelectrochemical water splitting and catalysts. However, the

fundamentals of the sol-flame methods, especially the key factor of formation the final morphologies, are not clear so far. There are several questions to be addressed.

a). The relations between the metal salt and the final morphology

The precursor salts so far are limited to acetate salts. It is proposed that the NP chain structure is related to the gaseous products formed at high temperatures from the decomposition of the metal salts. This point should be further clarified by changing the metal salts precursors to inorganic metal salts and other organ metallic salts.

b). The relations between the solvent and the final morphology

Another key factor for the formation of NP chains is the solvent. Similar to the metal salt precursor, the remaining solvent also gives rise to the gaseous products in flame. Considering the amount, the solvents may have more impact than the metal salt precursors. To complete the study, together with a), different solvents should also be studied. Several properties are essential for the solvents:

- Solubility of the metal salt in it and the viscosity. This is related to the amount of salt can be coated on the NWs.

- The number of C atoms. This is related to the amount of gaseous produced.

- The heat of combustion. This may impact the decomposition of metal salts and the nucleation of metal oxide NPs.

- The amount of solvent remained on the NWs. This is related to both the heat released and the gaseous products formed, and can be roughly controlled by air drying and pre-heating.

c).   The inert nature of the materials

It is found that for different materials, the easiness of the NP chain formation and the final morphology varies. For example, ZnO and Co_3O_4 tend to form the chain structure with high coverage density, while NiO yields lower density at the same condition. It is a more complicated problem to address, both experiments and simulation need to be done.

7.2.4. Sol-flame method to dope NWs

The doped NWs are attractive in a wide range of applications. The sol-flame method is a simple and neat ex-situ doping method, enables delicate substrates and prevents original crystallinity changes. With the sol-flame method, we have successfully doped TiO_2 NRs with W, which has shown enhanced performance in photoelectrochemical water splitting (Chapter 6). It is worth efforts to extend this method to other important functional materials, such as p-type ZnO, Ti doped Fe_2O_3, In doped SnO, etc. .

Moreover, together with Section 7.2.3, simulation of the formation the dopants or NP chains in different NWs should also be done to confirm and explain the experimental results.

Bibliography

[1] http://goldbook.iupac.org/C00876.html

[2] J. N. Armor, Appl. Catal., A 222 (1-2) (2001) 407-426.

[3] Bell, A. T, in: Catalysis Looks to the Future, National Academy Press: Washington, D.C., 1992; p 96.

[4] R. L. Burwell, Pure and Applied Chemistry 46 (1) (1976) 71-90.

[5] J. A. Dumesic, G. W. Huber, M. Boudart, in: Handbook of Heterogeneous Catalysis, Wiley-VCH Verlag GmbH & Co. KGaA: 2008.

[6] S. Brunauer, P. H. Emmett, E. Teller, J. Am. Chem. Soc. 60 (2) (1938) 309-319.

[7] N. A. Seaton, J. P. R. B. Walton, N. quirke, Carbon 27 (6) (1989) 853-861.

[8] C. Lastoskie, K. E. Gubbins, N. Quirke, J. Phys. Chem. 97 (18) (1993) 4786-4796.

[9] F. R.-R. K. S. W. S. J. Rouquerol, K. K. Unger, in: Studies in Surface Science and Catalysis, Elsevier: 1994; Vol. Volume 87, pp 798-802.

[10] P. B. Wells, Applied Catalysis 18 (2) (1985) 259-272.

[11] R. J. Matyi, L. H. Schwartz, J. B. Butt, Catalysis Reviews 29 (1) (1987) 41-99.

[12] G. A. Martin, B. Moraweck, A. J. Renouprez, G. Dalmai-Imelik, B. Imelik, Journal de Chimie Physique et de Physico-Chimie Biologique 69 (3) (1972) 532.

[13] J. Haber, J. H. Block, B. Delmon, in: Handbook of Heterogeneous Catalysis, Wiley-VCH Verlag GmbH & Co. KGaA: 2008.

[14] P. D. Garn, Thermoanalytical Methods of Investigation, Academic Press, New York, 1965, p.^pp. 1.

[15] S. D. Robertson, B. D. McNicol, J. H. De Baas, S. C. Kloet, J. W. Jenkins, J. Catal. 37 (3) (1975) 424-431.

[16] R. B. Anderson, K. C. Stein, J. J. Feenan, L. J. E. Hofer, Industrial and Engineering Chemistry 53 (10) (1961) 809-812.

[17] D. L. Trimm, Applied Catalysis 7 (3) (1983) 249-282.

[18] R. Prasad, L. A. Kennedy, E. Ruckenstein, Catal. Rev.-Sci. Eng. 26 (1) (1984) 1-58.

[19] M. F. M. Zwinkels, S. G. Jaras, P. G. Menon, T. A. Griffin, Catal. Rev.-Sci. Eng. 35 (3) (1993) 319-358.

[20] J. P. Coutures, J. M. Badie, R. Berjoan, J. Coutures, R. Flamand, A. Rouanet, High Temperature Science 13 (1-4) (1980) 331-336.

[21] J. Kirchnerova, Korean Journal of Chemical Engineering 16 (4) (1999) 427-433.

[22] A. Nishino, Catalysis Today 10 (1) (1991) 107-118.

[23] R. Prasad, L. A. Kennedy, E. Ruckenstein, Combustion Science and Technology 27 (1-2) (1981) 45-54.

[24] R. Prasad, L. A. Kennedy, E. Ruckenstein, Combustion Science and Technology 22 (5-6) (1980) 271-280.

[25] P. Gelin, M. Primet, Appl. Catal., B 39 (1) (2002) 1-37.

[26] D. W. Johnson, P. K. Gallagher, G. K. Wertheim, E. M. Vogel, J. Catal. 48 (1-3) (1977) 87-97.

[27] M. V. Twigg, Appl. Catal., B 70 (1-4) (2007) 2-15.

[28] H. Arai, T. Yamada, K. Eguchi, T. Seiyama, Applied Catalysis 26 (1-2) (1986) 265-276.

[29] Z. R. Ismagilov, M. A. Kerzhentsev, Catal. Rev.-Sci. Eng. 32 (1-2) (1990) 51-103.

[30] P. Briot, M. Primet, Applied Catalysis 68 (1-2) (1991) 301-314.

[31] P. Briot, A. Auroux, D. Jones, M. Primet, Applied Catalysis 59 (1) (1990) 141-152.

[32] R. F. Hicks, H. Qi, M. L. Young, R. G. Lee, W. J. Han, A. B. Kooh, Chemical Engineering Science 45 (8) (1990) 2647-2651.

[33] R. F. Hicks, H. H. Qi, M. L. Young, R. G. Lee, J. Catal. 122 (2) (1990) 295-306.

[34] Y. Morooka, Y. Morikawa, A. Ozaki, J. Catal. 7 (1) (1967) 23.

[35] Y. Morooka, A. Ozaki, J. Catal. 5 (1) (1966) 116.

[36] J. Liu, Z. Zhao, C. M. Xu, A. J. Duan, L. Wang, S. J. Zhang, Catal. Commun. 8 (3) (2007) 220-224.

[37] M. Faticanti, N. Cioffi, S. De Rossi, N. Ditaranto, P. Porta, L. Sabbatini, T. Bleve-Zacheo, Appl. Catal., B 60 (1-2) (2005) 73-82.

[38] R. Schlogl, S. B. Abd Hamid, Angewandte Chemie-International Edition 43 (13) (2004) 1628-1637.

[39] R. Zanella, S. Giorgio, C. H. Shin, C. R. Henry, C. Louis, J. Catal. 222 (2) (2004) 357-367.

[40] N. Toshima, Y. Shiraishi, T. Teranishi, M. Miyake, T. Tominaga, H. Watanabe, W. Brijoux, H. Bonnemann, G. Schmid, Appl. Organomet. Chem. 15 (3) (2001) 178-196.

[41] M. C. Marion, E. Garbowski, M. Primet, J. Chem. Soc., Faraday Trans. 87 (11) (1991) 1795-1800.

[42] G. Aguila, F. Gracia, J. Cortes, P. Araya, Appl. Catal., B 77 (3-4) (2008) 325-338.

[43] P. W. Park, J. S. Ledford, Applied Catalysis B-Environmental 15 (3-4) (1998) 221-231.

[44] T. J. Huang, K. C. Lee, H. W. Yang, W. P. Dow, Appl. Catal., A 174 (1-2) (1998) 199-206.

[45] L. Kundakovic, M. Flytzani-Stephanopoulos, Appl. Catal. A-Gen. 171 (1) (1998) 13-29.

[46] M. K. Dongare, V. Ramaswamy, C. S. Gopinath, A. V. Ramaswamy, S. Scheurell, M. Brueckner, E. Kemnitz, J. Catal. 199 (2) (2001) 209-216.

[47] P. Artizzu, E. Garbowski, M. Primet, Y. Brulle, J. Saint-Just in: *Catalytic combustion of methane on aluminate-supported copper oxide*, 1999; Elsevier Science Bv: 1999; pp 83-93.

[48] N. Guilhaume, M. Primet, J. Chem. Soc., Faraday Trans. 90 (11) (1994) 1541-1545.

[49] F. G. Dwyer, Catalysis Reviews 6 (2) (1972) 261-&.

[50] J. Huang, S. R. Wang, Y. Q. Zhao, X. Y. Wang, S. P. Wang, S. H. Wu, S. M. Zhang, W. P. Huang, Catalysis Communications 7 (12) (2006) 1029-1034.

[51] W. Liu, M. Flytzani-Stephanopoulos, Chemical Engineering Journal 64 (2) (1996) 283-294.

[52] G. A. El-Shobaky, F. M. Radwan, A. E. M. Turky, A. A. El-Moemen, Adsorption Science & Technology 19 (10) (2001) 779-793.

[53] X. S. Huang, H. Sun, L. C. Wang, Y. M. Liu, K. N. Fan, Y. Cao, Appl. Catal., B 90 (1-2) (2009) 224-232.

[54] M. A. Albiter, R. Huirache-Acuna, F. Paraguay-Delgado, F. Zaera, G. Alonso-Nunez, Journal of Nanoscience and Nanotechnology 8 (12) (2008) 6437-6444.

[55] T. Maiyalagan, B. Viswanathan, Journal of Power Sources 175 (2) (2008) 789-793.

[56] X. W. Xie, Y. Li, Z. Q. Liu, M. Haruta, W. J. Shen, Nature 458 (7239) (2009) 746-749.

[57] R. Xu, X. Wang, D. S. Wang, K. B. Zhou, Y. D. Li, J. Catal. 237 (2) (2006) 426-430.

[58] S. H. Liang, F. T. G. Bulgan, R. L. Zong, Y. F. Zhu, J. Phys. Chem. C 112 (14) (2008) 5307-5315.

[59] Y. Zhang, A. Kolmakov, Y. Lilach, M. Moskovits, J. Phys. Chem. B 109 (5) (2005) 1923-1929.

[60] Y. Zhang, A. Kolmakov, S. Chretien, H. Metiu, M. Moskovits, Nano Lett. 4 (3) (2004) 403-407.

[61] L. Wang, Y. F. Zhu, J. Phys. Chem. B 109 (11) (2005) 5118-5123.

[62] L. Gonzalez-Rovira, J. M. Sanchez-Amaya, M. Lopez-Haro, E. del Rio, A. B. Hungria, P. Midgley, J. J. Calvino, S. Bernal, F. J. Botana, Nano Lett. 9 (6) (2009) 2511-2511.

[63] L. Wang, B. Peng, X. F. Guo, W. P. Ding, Y. Chen, Chemical Communications (12) (2009) 1565-1567.

[64] A. Kolmakov, M. Moskovits, Ann. Rev. Mater. Res. 34) (2004) 151-180.

[65] J. H. Zeng, B. B. Jin, Y. F. Wang, Chem. Phys. Lett. 472 (1-3) (2009) 90-95.

105

[66] n. The surface area of the copper mesh is 767 cm^2. The mass of catalyst is 16.5 g. The CuO NWs on average are about 50 μm long, 100 nm in diameter with a coverage density of 10^8/cm^2. Assuming that the NWs are cylinders, the specific surface area (SSA) was estimated by

$$\text{SSA} = \frac{\text{total surface area}}{\text{total mass}} = \frac{\pi \times 100\,\text{nm} \times 50\,\mu\text{m} \times 10^8/\text{cm}^2 \times 767\,\text{cm}^2 + 767\,\text{cm}^2}{16.5\,\text{g}} \approx 0.08\,\text{m}^2/\text{g}$$

[67] G. Marban, I. Lopez, T. Valdes-Solis, A. B. Fuertes, International Journal of Hydrogen Energy 33 (22) (2008) 6687-6695.

[68] G. Marban, A. Lopez, I. Lopez, T. Valdes-Solis, Applied Catalysis B: Environmental 99 (1-2) (2010) 257-264.

[69] M. C. Marion, E. Garbowski, M. Primet, Journal of the Chemical Society-Faraday Transactions 86 (17) (1990) 3027-3032.

[70] A. Martinez-Arias, M. Fernandez-Garcia, O. Galvez, J. M. Coronado, J. A. Anderson, J. C. Conesa, J. Soria, G. Munuera, Journal of Catalysis 195 (1) (2000) 207-216.

[71] B. Skarman, D. Grandjean, R. E. Benfield, A. Hinz, A. Andersson, L. R. Wallenberg, Journal of Catalysis 211 (1) (2002) 119-133.

[72] S. M. Zhang, W. P. Huang, X. H. Qiu, B. Q. Li, X. C. Zheng, S. H. Wu, Catalysis Letters 80 (1-2) (2002) 41-46.

[73] X. L. Tang, B. C. Zhang, Y. Li, Y. D. Xu, Q. Xin, W. J. Shen, Catalysis Today 93-5) (2004) 191-198.

[74] M. F. Luo, J. M. Ma, J. Q. Lu, Y. P. Song, Y. J. Wang, Journal of Catalysis 246 (1) (2007) 52-59.

[75] D. Chen, G. Shen, K. Tang, Y. Qian, Journal of Crystal Growth 254 (1-2) (2003) 225-228.

[76] C.-T. Hsieh, J.-M. Chen, H.-H. Lin, H.-C. Shih, Applied Physics Letters 82 (19) (2003) 3316-3318.

[77] M. H. Cao, C. W. Hu, Y. H. Wang, Y. H. Guo, C. X. Guo, E. B. Wang, Chemical Communications (15) (2003) 1884-1885.

[78] P. M. Rao, X. L. Zheng, Nano Lett. 9 (8) (2009) 3001-3006.

[79] X. C. Jiang, T. Herricks, Y. N. Xia, Nano Letters 2 (12) (2002) 1333-1338.

[80] C. H. Xu, C. H. Woo, S. Q. Shi, Chem. Phys. Lett. 399 (1-3) (2004) 62-66.

[81] Y. W. Zhu, T. Yu, F. C. Cheong, X. J. Xui, C. T. Lim, V. B. C. Tan, J. T. L. Thong, C. H. Sow, Nanotechnology 16 (1) (2005) 88-92.

[82] M. A. Vannice, Catalysis Today 123 (1-4) (2007) 18-22.

[83] P. Mars, D. W. Van Krevelen, Chemical Engineering and Science Special Supply) (1954) 41.

[84] The mass of Cu in the CuO NWs was calculated by adopting the same assumptions as for surface area. The density of CuO is 6.31g/cm^3. Therefore,

$$\text{Mass}_{\text{CuO}} = \rho \cdot V = 6.31 \,\text{g/cm}^3 \times \pi \times (100 \,\text{nm/2})^2 \times 50 \,\mu\text{m} \times 10^8 /\text{cm}^2 \times 767 \,\text{cm}^2 \approx 0.19 \,\text{g}$$

$$\text{Mass}_{\text{Cu}} = \text{Mass}_{\text{CuO}} \times (64/80) = 0.15 \,\text{g}$$

[85] Y. Feng, P. M. Rao, D. R. Kim, X. Zheng, Proc. Combust. Inst. 33 (2) (2010) 3169-3175.

[86] J. Van Durme, J. Dewulf, C. Leys, H. Van Langenhove, Applied Catalysis B: Environmental 78 (3-4) (2008) 324-333.

[87] T. J. Huang, D. H. Tsai, Catalysis Letters 87 (3-4) (2003) 173-178.

[88] G. G. Jernigan, G. A. Somorjai, Journal of Catalysis 147 (2) (1994) 567-577.

[89] B. White, M. Yin, A. Hall, D. Le, S. Stolbov, T. Rahman, N. Turro, S. O'Brien, Nano Letters 6 (9) (2006) 2095-2098.

[90] V. A. Sadykov, S. F. Tikhov, N. N. Bulgakov, A. P. Gerasev, Catalysis Today 144 (3-4) (2009) 324-333.

[91] D. Le, S. Stolbov, T. S. Rahman, Surface Science 603 (10-12) (2009) 1637-1645.

[92] Y. Qin, T. Staedler, X. Jiang, Nanotechnology 18 (3) (2007)

[93] U. R. Pillai, S. Deevi, Applied Catalysis B-Environmental 64 (1-2) (2006) 146-151.

[94] W. Shi, N. Chopra, J. Nanopart. Res. 13 (2) (2011) 851-868.

[95] C.-H. Lin, J.-H. Chao, C.-H. Liu, J.-C. Chang, F.-C. Wang, Langmuir 24 (17) (2008) 9907-9915.

[96] Y. Tak, S. J. Hong, J. S. Lee, K. Yong, Cryst. Growth Des. 9 (6) (2009) 2627-2632.

[97] P. L. Taberna, S. Mitra, P. Poizot, P. Simon, J. M. Tarascon, Nat. Mater. 5 (7) (2006) 567-573.

[98] V. V. Dobrokhotov, D. N. McIlroy, M. G. Norton, R. Abdelrahaman, A. Safir, C. A. Berven, Nanotechnology 20 (13) (2009) 135504.

[99] Y. Zhang, J. Xu, P. Xu, Y. Zhu, X. Chen, W. Yu, Nanotechnology 21 (28) (2010) 285501.

[100] Y. Xie, K. Ding, Z. Liu, R. Tao, Z. Sun, H. Zhang, G. An, J. Am. Chem. Soc. 131 (19) (2009) 6648-6649.

[101] Y. Lin, D. W. Baggett, J.-W. Kim, E. J. Siochi, J. W. Connell, ACS Appl. Mat. Interfaces 3 (5) (2011) 1652-1664.

[102] M. J. Height, L. Madler, S. E. Pratsinis, F. Krumeich, Chem. Mater. 18 (2) (2005) 572-578.

[103] F. Xu, X. Liu, S. D. Tse, F. Cosandey, B. H. Kear, Chem. Phys. Lett. 449 (1-3) (2007) 175-181.

[104] W. Merchan-Merchan, A. V. Saveliev, A. M. Taylor, Nanotechnology 19 (12) (2008)

[105] P. M. Rao, X. Zheng, Proc. Combust. Inst. 33 (2) (2011) 1891-1898.

[106] L. Cai, P. M. Rao, X. Zheng, Nano Lett. 11 (2) (2011) 872-877.

[107] P. M. Rao, X. Zheng, Nano Lett. 11 (6) (2011) 2390-2395.

[108] S. E. Pratsinis, Prog. Energy Combust. Sci. 24 (3) (1998) 197-219.

[109] W. Hartmann, A. T. Liu, D. Peuckert, P. Kleinschmit, Mater. Sci. Eng., A 109 (C) (1989) 243-246.

[110] C.-H. Hung, J. L. Katz, J, Mater. Res. 7 (7) (1992) 1861-1869.

[111] B. D. Merkle, R. N. Kniseley, F. A. Schmidt, I. E. Anderson, Mater. Sci. Eng., A 124 (1) (1990) 31-38.

[112] L. L. Hench, J. K. West, Chem. Rev. 90 (1) (1990) 33-72.

[113] L. Madler, H. K. Kammler, R. Mueller, S. E. Pratsinis, J. Aerosol Sci. 33 (2) (2002) 369-389.

[114] R. Strobel, A. Baiker, S. E. Pratsinis, Adv. Powder Technol. 17 (5) (2006) 457-480.

[115] W. Y. Teoh, R. Amal, L. Madler, Nanoscale 2 (8) (2010) 1324-1347.

[116] R. Strobel, S. E. Pratsinis, Phys. Chem. Chem. Phys. 13 (20) (2011) 9246-9252.

[117] Y. Feng, X. Zheng, Nano Lett. 10 (11) (2010) 4762-4766.

[118] T. V. Choudhary, S. Banerjee, V. R. Choudhary, Appl. Catal. A-Gen. 234 (1-2) (2002) 1-23.

[119] Y. Feng, X. Zheng, ChemCatChem) (2012) n/a-n/a.

[120] W. Zhou, C. Cheng, J. Liu, Y. Y. Tay, J. Jiang, X. Jia, J. Zhang, H. Gong, H. H. Hng, T. Yu, H. J. Fan, Adv. Funct. Mater. 21 (13) (2011) 2439-2445.

[121] S. Zhou, X. Liu, D. Wang, Nano Lett. 10 (3) (2010) 860-863.

[122] M. J. Bierman, S. Jin, Energy Environ. Sci. 2 (10) (2009) 1050-1059.

[123] H. Wang, Y. Bai, H. Zhang, Z. Zhang, J. Li, L. Guo, J. Phys. Chem. C 114 (39) (2010) 16451-16455.

[124] X. H. Chen, M. Moskovits, Nano Lett. 7 (3) (2007) 807-812.

[125] J. G. Yu, Q. J. Xiang, M. H. Zhou, Appl. Catal., B 90 (3-4) (2009) 595-602.

[126] I. S. Cho, Z. Chen, A. J. Forman, D. R. Kim, P. M. Rao, T. F. Jaramillo, X. Zheng, Nano Lett. 11 (11) (2011) 4978-4984.

[127] A. V. Shchenev, Y. F. Kargin, V. M. Skorikov, Russ. J. Inorg. Chem. 33) (1988) 1237-1238.

[128] G. J. French, F. R. Sale, J. Mater. Sci. 20 (4) (1985) 1291-1300.

[129] E. Prince, R. G. Treuting, Acta Crystallogr. 9 (12) (1956) 1025-1028.

[130] W. Choi, A. Termin, M. R. Hoffmann, J. Phys. Chem. 98 (51) (1994) 13669-13679.

[131] Y. Cong, J. Zhang, F. Chen, M. Anpo, D. He, J. Phys. Chem. C 111 (28) (2007) 10618-10623.

[132] Y. Zhang, S. G. Ebbinghaus, A. Weidenkaff, T. Kurz, H. A. K. Von Nidda, P. J. Klar, M. Gungerich, A. Rellert, Chem. Mater. 15 (21) (2003) 4028-4033.

[133] J. A. Navio, G. Colon, M. Trillas, J. Peral, X. Domenech, J. J. Testa, J. Padron, D. Rodriguez, M. I. Litter, Appl. Catal., B 16 (2) (1998) 187-196.

[134] Y. Li, B. Tan, Y. Wu, Journal of the American Chemical Society 128 (44) (2006) 14258-14259.

[135] Y. Li, B. Tan, Y. Wu, Nano Letters 8 (1) (2007) 265-270.

[136] T. Herricks, J. Chen, Y. Xia, Nano Letters 4 (12) (2004) 2367-2371.

[137] M. Kokotov, A. Biller, G. Hodes, Chemistry of Materials 20 (14) (2008) 4542-4544.

[138] M. Kokotov, G. Hodes, Chemistry of Materials 22 (19) (2010) 5483-5491.

[139] D. B. Li, X. H. Liu, Q. H. Zhang, Y. Wang, H. L. Wan, Catalysis Letters 127 (3-4) (2009) 377-385.

[140] G. Fierro, M. Lo Jacono, M. Inversi, R. Dragone, P. Porta, Topics in Catalysis 10 (1-2) (2000) 39-48.

[141] M. J. Pollard, B. A. Weinstock, T. E. Bitterwolf, P. R. Griffiths, A. Piers Newbery, J. B. Paine Iii, Journal of Catalysis 254 (2) (2008) 218-225.

[142] T. Nitadori, T. Ichiki, M. Misono, Bulletin of the Chemical Society of Japan 61 (3) (1988) 621-626.

111

[143] B. Decollongue, E. Garbowski, M. Primet, J. Chem. Soc., Faraday Trans. 87 (15) (1991) 2493-2499.

[144] X. H. Zhu, Z. G. Liu, N. B. Ming, Journal of Nanoscience and Nanotechnology 10 (7) (2010) 4109-4123.